Slip over liquid-infused gratings in the singular limit of a nearly inviscid lubricant

Gunnar G. Peng [1], Ehud Yariv [2,3] and Ory Schnitzer [4]

[1] *Department of Mathematics, University College London, London WC1E 6BT, United Kingdom*

[2] *Department of Mathematics, Technion—Israel Institute of Technology, Haifa 32000, Israel*

[3] *Department of Mechanical and Aerospace Engineering, Princeton University, Princeton, New Jersey 08544, USA*

[4] *Department of Mathematics, Imperial College London, London SW7 2AZ, United Kingdom*

(Received 10 August 2025; accepted 27 February 2026; published 6 April 2026)

We consider shear-driven longitudinal flow of an exterior fluid over a periodic array of rectangular grooves filled with an immiscible interior fluid (the "lubricant"), the grooves being formed by infinitely thin ridges protruding from a flat substrate. The ratio λ of the effective slip length to the semiperiod is a function of the ratio μ of the interior to exterior viscosities and the ratio h of the groove depth to the semiperiod. We focus on the limit $\mu \ll 1$, which is singular for that geometry. We find that the viscous resistance to the imposed shear is dominated by a boundary layer of exponentially small extent about the ridge tips, resulting in the effective slip length scaling as $\mu^{-1/2}$—not μ^{-1} as implied by intuitive arguments overlooking the tip contributions (and by proposed approximations in the literature). Analyzing that exponential region in conjunction with an integral force balance, we find the simple asymptotic approximation $\lambda \approx \mu^{-1/2}$; using conformal mappings, we also calculate the leading-order correction to that result, which introduces a dependence upon h. The ensuing asymptotic expansion breaks down for $h = O(\mu^{1/2})$, upon transitioning to a lubrication geometry. We accordingly conduct a companion asymptotic analysis in the distinguished limit of small μ and fixed $H = h/\mu^{1/2}$, which gives $\lambda \approx \mu^{-1/2} H/(1+H)$ as well as a closed-form leading-order correction to that approximation; the intuitive μ^{-1} scaling is accordingly only relevant to the regime $H \ll 1$ corresponding to extremely shallow grooves. We demonstrate excellent agreement between our predictions and numerical solutions constructed using a boundary-integral formulation.

DOI: 10.1103/kr2n-ckjv

I. INTRODUCTION

There is continued interest in the use of engineered microstructured surfaces to reduce hydrodynamic resistance at small scales. Such drag reduction typically hinges upon the stable entrapment of a relatively inviscid lubricant within the microstructure cavities. Traditionally, research has focused on superhydrophobic surfaces [1,2]: made of or coated with hydrophobic materials, and characterized by small-scale roughness, either random or periodic. When these surfaces come into contact with liquid, air becomes trapped in a Cassie state within the cavities, creating a composite surface consisting of the solid substrate and the liquid-air menisci [3]. Recently, a promising alternative has emerged: slippery liquid-infused porous surfaces (SLIPS), which are designed to spontaneously

Published by the American Physical Society under the terms of the Creative Commons Attribution 4.0 International license. Further distribution of this work must maintain attribution to the author(s) and the published article's title, journal citation, and DOI.

imbibe a liquid lubricant through wicking [4–6]. While the liquid lubricant cannot match air's low viscosity, SLIPS generally offer superior robustness compared with superhydrophobic surfaces.

Toward characterizing the drag-reduction efficacy of a given microstructured surface, it is expedient to consider a canonical problem [7] where the liquid adjacent to the surface is exposed to a far-field simple shear flow, parallel to the surface,

$$\mathbf{u}_* \sim \hat{\mathbf{s}}\, G_* y_* \quad \text{as} \quad y_* \to \infty, \tag{1.1}$$

where y_* is the distance from the surface, G_* is the shear rate of the imposed flow, and $\hat{\mathbf{s}}$ is its direction. (Henceforth, an asterisk subscript denotes a dimensional quantity.) Since the imposed flow (1.1) vanishes at $y_* = 0$, it constitutes an exact solution in the case of a smooth solid surface. The microstructure modifies that flow, inducing a uniform "slip" stream, say, $\mathbf{u}_*^s$, at large distances, whereby the far-field expansion (1.1) extends as

$$\mathbf{u}_* = \hat{\mathbf{s}}\, G_* y_* + \mathbf{u}_*^s + o(1) \quad \text{as} \quad y_* \to \infty. \tag{1.2}$$

With negligible inertia, the flow is governed by the linear Stokes equations. Assuming that the shape of the menisci is determined by capillarity (and, in particular, is essentially unaffected by the flow), the entire problem is linear and homogeneous in $\hat{\mathbf{s}}G_*$. The slip velocity must therefore possess the form $\mathbf{u}_*^s = G_* \boldsymbol{\lambda}_* \cdot \hat{\mathbf{s}}$, wherein the effective slip length $\boldsymbol{\lambda}_*$ is a two-dimensional (2D) second-order tensor depending on the surface geometry and the viscosity ratio of the two fluids. The most common microstructure configuration, used for both superhydrophobic surfaces and SLIPS, consists of a periodic array of ridges protruding perpendicularly from a flat solid substrate, with the lubricant filling the resulting grooves (of rectangular cross section). For such configurations, the effective slip length adopts the simplified anisotropic form $\boldsymbol{\lambda} = \lambda_*^{\parallel} \hat{\mathbf{e}}_3 \hat{\mathbf{e}}_3 + \lambda_*^{\perp} \hat{\mathbf{e}}_1 \hat{\mathbf{e}}_1$, in which the longitudinal slip length $\lambda_*^{\parallel}$ and transverse slip length $\lambda_*^{\perp}$ can be independently found by considering independent flow problems where the shear is applied parallel ($\hat{\mathbf{s}} = \hat{\mathbf{e}}_3$) or perpendicular to the ridges ($\hat{\mathbf{s}} = \hat{\mathbf{e}}_1$), respectively.

Given the minute viscosity of air, the menisci of superhydrophobic surfaces have traditionally been modeled as free surfaces [8]. The canonical effective-slip problem then reduces to a liquid-flow problem, decoupled from the flow inside the cavities. Accordingly, the microstructure geometry is manifested only through the partitioning of the liquid boundary into solid-liquid and gas-liquid interfaces. Assuming flat menisci, the imposed far-field stress is resisted only by viscous shear stresses at the solid-liquid interfaces. Hence, the limit where the solid fraction of the compound liquid interface vanishes is singular. In particular, the effective slip length diverges in that limit. The rate of this divergence—scaling logarithmically with the solid fraction for grooved or meshed surfaces, or algebraically for post arrays—has been elucidated through numerous analytical and asymptotic studies [9–19]. While giant slip lengths have indeed been reported using small-solid-fraction superhydrophobic surfaces [20,21], the prospects of such surfaces are considered limited since the Cassie state inevitably collapses if the solid fraction is too low [22–24].

Unlike in the superhydrophobic scenario, models of flow over SLIPS typically account for a finite lubricant viscosity. The effective-slip problem then involves the coupling of the exterior flow outside the cavities and the lubricant flow inside them. This coupling introduces a dependency not just on the viscosity ratio of the two fluids, but also on the interior geometry of the microstructure cavities; for "rectangular" grooves, the extra geometric parameter, in addition to the solid fraction, is the ridge height (i.e., groove depth). Very few analytical studies of the effective-slip problem have included the effect of the interior fluid. The only systematic analysis we are aware of is that of Crowdy [25], who derived analytical formulas for the effective slip length by perturbing about Philip's classical complex-variable solutions for an inviscid lubricant [26]. Other investigators, including Schönecker *et al.* [27] and Nizkaya *et al.* [28], have employed a mix of exact solutions and heuristic modeling assumptions, demonstrating good agreement with numerical simulations over a wide parameter range.

Having a finite lubricant viscosity regularizes the small-solid-fraction singularity. Indeed, the imposed shear is then resisted not just by the exterior solid boundaries, as in the superhydrophobic scenario, but also by the liquid-liquid interfaces. (Alternatively, one could interpret this as the imposed shear being resisted by both the exterior and interior solid boundaries.) Although the effective slip length no longer diverges as the solid fraction vanishes, it is still expected to increase in magnitude in that limit. Moreover, from a practical viewpoint, the SLIPS are stable even at very low solid fraction [29]. This motivates theoretical analysis of idealized *zero-solid-fraction* configurations. In particular, it is natural to consider the ubiquitous rectangular-groove geometry in the case of zero-thickness ridges—henceforth referred to as a "grating." Indeed, this geometry has been studied in both the transverse problem [30] and the longitudinal problem [31]. (The latter problem was actually studied for a single-phase flow, corresponding to the special case where the viscosities are matched.) This geometry has also been employed by Yan and Kowal [32] in an analysis of transverse flow over a liquid-infused surface, with the effective slip length estimated using a heuristic approach similar to those of Schönecker *et al.* [27] and Nizkaya *et al.* [28].

For the zero-solid-fraction grating geometry, the imposed shear is entirely supported by the lubricant. Accordingly, this scenario introduces a new *singular* limit in which the effective slip length diverges: that where the lubricant viscosity is vanishingly small. This previously unexplored singular limit is practically significant as it characterizes the maximum potential for drag reduction of SLIPS. As such, the motivation for studying it parallels that for the singular small-solid-fraction limit of the inviscid-lubricant scenario. In light of the above, the majority of our paper is concerned with an asymptotic analysis of the grating geometry in the singular limit of a nearly inviscid lubricant. We focus on the longitudinal grating problem, which is simpler and associated with larger slip lengths than its transverse counterpart. Similarly to analyses of the above-mentioned small-solid-fraction limit, we employ matched asymptotic expansions [33] in conjunction with conformal mappings [34].

While the singular nature of the nearly inviscid limit is evident, the corresponding scaling of the effective slip length is not. Let λ_* denote this length, and $\mu = \mu_*^-/\mu_*^+$ the ratio of the interior to exterior viscosities. By an integral force balance, the imposed shear stress $\mu_*^+ G_*$ must balance the average stress at the liquid-liquid interface. In the limit $\mu \ll 1$, it is intuitive to anticipate that the exterior flow is dominated by a uniform slip stream, which in light of Eq. (1.2) should be of magnitude $v_* = G_*\lambda_*$. Since the velocity is continuous at the interface, the interfacial shear stress can be estimated as $\mu_*^- v_*/\ell_*$, where ℓ_* is a length scale characterizing the interior flow (say the groove width). This argument, which follows the classical scaling approach of Ybert *et al.* [11], yields the singular scaling $\lambda_*/\ell_* = \mathrm{ord}(1/\mu)$. This scaling is built into Yan and Kowal's model for slip over a grating geometry [32]. Some scrutiny reveals that it is also predicted by the more general models proposed by Schönecker *et al.* [27] and Nizkaya *et al.* [28], when these are degenerated to a grating geometry and reduced in the nearly inviscid limit.

Nonetheless, our analysis will reveal that the μ^{-1} scaling is actually *erroneous*, except in a lubricationlike limit corresponding to extremely shallow grooves. Indeed, the above scaling arguments overlook the formation of boundary layers, of *exponentially small* extent, about the tips of the zero-thickness ridges. At leading order, the applied shear is entirely supported by the localized flow in these tip regions. This delicate balance, in turn, implies an effective slip length that turns out to scale as $\mu^{-1/2}$.

The paper is arranged as follows. In the next section we formulate the problem for longitudinal shear flow about a grating and derive a useful integral force balance. We also briefly discuss a numerical scheme used to solve this "exact" problem. The intuitive lubrication limit corresponding to shallow grooves is briefly addressed in Sec. III. In preparation for the analysis of the singular limit $\mu \ll 1$, we perform in Sec. IV a local analysis of the flow problem in the vicinity of the tips. The limit $\mu \ll 1$ is analyzed in Sec. V, where the identification and analysis of the localized tip layers furnish the leading-order slip length. In Sec. VI we derive a functional expression for the ord(1) correction to the slip length. In Sec. VII we identify a distinguished limit of shallow grooves and a nearly inviscid lubricant and calculate the associated

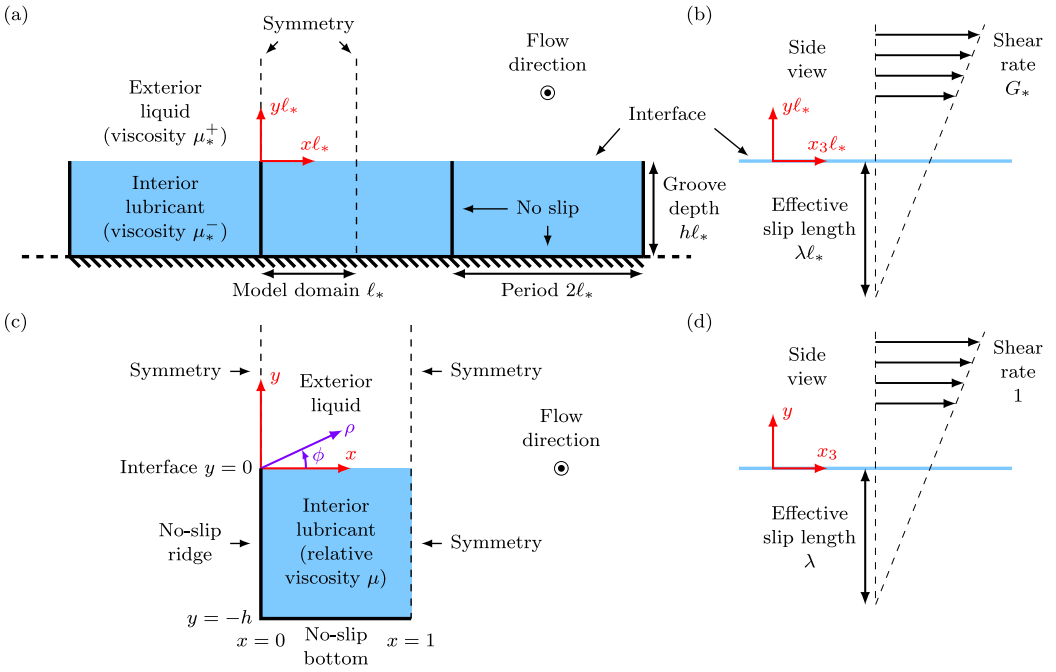


FIG. 1. Schematics showing [(a), (b)] dimensional and [(c), (d)] dimensionless quantities. In (c), only the model domain $0 < x < 1$ is shown.

slip length. We conclude in Sec. VIII, addressing deviations from a grating geometry to finite solid fractions.

II. PROBLEM FORMULATION

The problem is depicted in Figs. 1(a) and 1(b). The underlying solid substrate is a grating of period $2\ell_*$. The ridges are assumed infinitely thin; their height is $h\ell_*$. The grooves bounded by the ridges and the bottom substrate are filled with an "interior" lubricant, of viscosity μ_*^-. The resulting compound surface is brought into contact with an "exterior" liquid of viscosity μ_*^+. We assume that the menisci, pinned at the tips of the ridges, are flat (zero protrusion angle). At large distances from the surface, the flow approaches a longitudinal shear flow of shear-rate magnitude G_*; the velocity field thus satisfies the far-field condition (1.1), with the unit vector $\hat{\mathbf{s}}$ parallel to the grooves.

A. Dimensionless formulation

We utilize a dimensionless notation where length variables are normalized by ℓ_* and velocities by $\ell_* G_*$. We employ Cartesian coordinates $(x_1 = x,\ x_2 = y,\ x_3)$, with the imposed shear in the x_3-direction and the ridges located at $x = 2n$ with integer n. The plane $y = 0$ passes through the ridge tips; the exterior and interior fluids occupy the domains $y > 0$ and $-h < y < 0$, respectively. Since the flow is unidirectional, the velocity fields in the interior and exterior domains can be written as $\hat{\mathbf{e}}_3 w^{\pm}(x, y)$, where $\pm$ indicates the sign of y. Due to the discrete-translational (periodic) and mirror symmetries, it suffices to focus upon a single "semiunit cell," say, extending from the ridge at $x = 0$ to the center of the groove at $x = 1$ [see Fig. 1(c)].

The equations governing the velocity fields $w^{\pm}$ are then given as follows. Due to unidirectionality, the Navier-Stokes equations for the flows simplify to Laplace's equation in each domain:

$$\frac{\partial^2 w^{\pm}}{\partial x^2} + \frac{\partial^2 w^{\pm}}{\partial y^2} = 0 \quad \text{for} \quad y > 0\ (+) \quad \text{or} \quad -h < y < 0\ (-). \tag{2.1}$$

The two fields are linked by the interfacial conditions of continuous velocity,

$$w^+ = w^- \quad \text{at} \quad y = 0, \tag{2.2a}$$

and continuous shear stress,

$$\frac{\partial w^+}{\partial y} = \mu \frac{\partial w^-}{\partial y} \quad \text{at} \quad y = 0, \tag{2.2b}$$

where $\mu = \mu_*^-/\mu_*^+$. The interior field w^- further satisfies the symmetry condition

$$\frac{\partial w^-}{\partial x} = 0 \quad \text{at} \quad x = 1, \tag{2.3}$$

and the no-slip condition at the ridge and at the bottom,

$$w^- = 0 \quad \text{at} \quad x = 0, \qquad w^- = 0 \quad \text{at} \quad y = -h. \tag{2.4a,b}$$

The exterior field w^+ further satisfies the two symmetry conditions

$$\frac{\partial w^+}{\partial x} = 0 \quad \text{at} \quad x = 0, \qquad \frac{\partial w^+}{\partial x} = 0 \quad \text{at} \quad x = 1, \tag{2.5a,b}$$

the imposed shear in the far field,

$$w^+ \sim y \quad \text{as} \quad y \to \infty, \tag{2.6}$$

and the no-slip condition at the tip of the ridge,

$$\lim_{(x,y)\to(0,0)} w^+ = 0. \tag{2.7}$$

The problem posed by Eqs. (2.1)–(2.7) uniquely determines the flow fields $w^{\pm}(x, y)$, depending on the governing parameters μ and h. In particular, it determines the "slip length,"

$$\lambda = \lim_{y\to\infty} (w^+ - y), \tag{2.8}$$

namely, the constant correction to the shear in the far-field behavior [Eq. (2.6)]. That behavior is accordingly refined to [see Fig. 1(d)]

$$w^+ = y + \lambda + o(1) \quad \text{as} \quad y \to \infty. \tag{2.9}$$

The goal is to calculate λ as a function of μ and h.

B. Integral relations

It is useful to define the integral quantity

$$\mathcal{D} = \int_0^1 \left.\frac{\partial w^+}{\partial y}\right|_{y=0} dx, \tag{2.10a}$$

which can be interpreted as the net viscous drag exerted by the exterior fluid on the interior fluid, through viscous shear stresses at the interface. Using Eq. (2.2b), we can also express this drag in terms of the interior field as

$$\mathcal{D} = \mu \int_0^1 \left.\frac{\partial w^-}{\partial y}\right|_{y=0} dx. \tag{2.10b}$$

An integral force balance can be used to derive alternative expressions for $\mathcal{D}$. Let $\mathcal{C}$ be any simple curve in the exterior domain extending from the ray $x = 0$ to the ray $x = 1$. By integrating Laplace's equation (2.1) over the domain bounded between $y = 0$, the curve $\mathcal{C}$, and the rays $x = 0, 1$, and making use of the 2D variant of Gauss's theorem in conjunction with the symmetry conditions (2.5), we find

$$\mathcal{D} = \int_{\mathcal{C}} \hat{\mathbf{n}} \cdot \boldsymbol{\nabla} w^+ \, dl, \tag{2.11}$$

where $\hat{\mathbf{n}}$ is the unit normal to $\mathcal{C}$ pointing away from the domain, $\boldsymbol{\nabla} = \hat{\mathbf{e}}_1 \partial/\partial x + \hat{\mathbf{e}}_2 \partial/\partial y$ is the 2D gradient operator, and dl is the differential arclength along $\mathcal{C}$.

The viscous drag at the interface must balance the viscous tractions at large distances from the surface, which are set by the external shear flow. Indeed, following Schnitzer [14,15], we shift $\mathcal{C}$ to infinity in Eq. (2.11) and use the far-field condition (2.6) to find

$$\mathcal{D} = 1. \tag{2.12}$$

Substituting this result into Eqs. (2.10) and (2.11) gives the three equivalent integral balances

$$\int_0^1 \left. \frac{\partial w^+}{\partial y} \right|_{y=0} dx = 1, \qquad \mu \int_0^1 \left. \frac{\partial w^-}{\partial y} \right|_{y=0} dx = 1, \qquad \int_{\mathcal{C}} \hat{\mathbf{n}} \cdot \boldsymbol{\nabla} w^+ \, dl = 1. \tag{2.13a,b,c}$$

As these balances follow from the problem formulation, they do not provide independent constraints. Nonetheless, they will be found to be useful in the subsequent analysis. In particular, Eq. (2.13b) can be imposed on the interior field without the need to calculate the corresponding exterior solution.

We can also derive an integral expression for the slip length, expressed in terms of the velocity distribution at the interface. We first note from Eq. (2.11) that the drag definition (2.10a) can be generalized to arbitrary $y \geqslant 0$:

$$\mathcal{D} = \int_0^1 \frac{\partial w^+}{\partial y} \, dx. \tag{2.14}$$

Upon interchanging integration and differentiation, this extension gives

$$\mathcal{D} = \frac{d}{dy} \int_0^1 w^+(x, y) \, dx. \tag{2.15}$$

Then, by integrating Eq. (2.15) with respect to y, using Eq. (2.12) and the refined far-field behavior (2.9), and subsequently evaluating at $y = 0$, we find

$$\lambda = \int_0^1 w^+(x, 0) \, dy. \tag{2.16}$$

Our main goal in this paper is to derive approximations for the slip length λ in the limit $\mu \ll 1$, corresponding to a nearly inviscid lubricant. Prior to this, in Sec. III, we briefly consider the limit of shallow grooves, $h \ll 1$, and, in the subsequent Sec. IV, we perform a local analysis of the exact problem near the ridge tip. These preliminary steps will help guide our analysis and physical interpretation of the results.

We have also implemented a numerical scheme (see Appendix A for details) to solve a boundary-integral formulation of the governing equations (2.1)–(2.7), with the slip length evaluated from its integral representation (2.16). Figure 2 presents sample velocity fields for $\mu = 0.1$ and two values of h in detail, and the resulting slip length for various values of μ and h. The singularity of the limit $\mu \ll 1$ is evident. Further results are presented throughout the paper as a comparison with the results of our asymptotic analysis.

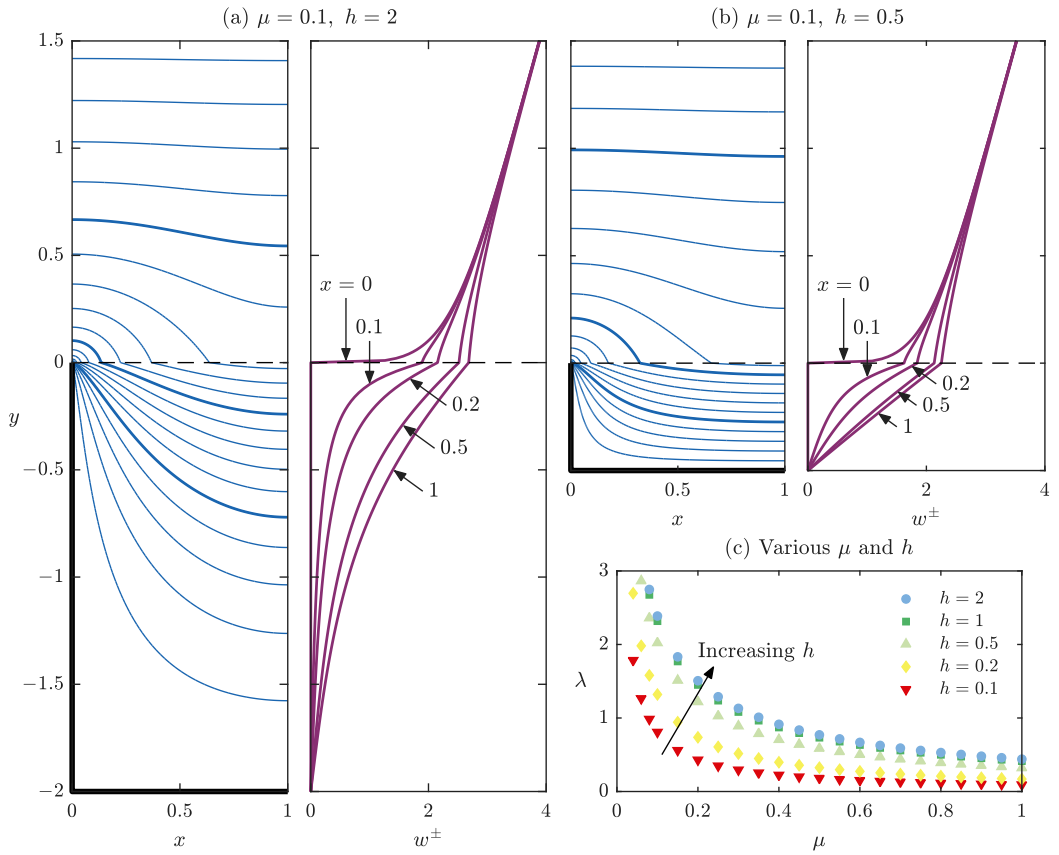


FIG. 2. Example numerical results. [(a) and (b)] Left: Contour plots of $w^{\pm}(x, y)$ with contour spacing $\Delta w = 0.2$ (thin contours) and $\Delta w = 1$ (thick contours); the no-slip walls [$w^{-} = 0$, see Eqs. (2.4)] are marked with thick black lines. Right: The $w^{\pm}$ profile at various values of x. The interior-to-exterior viscosity ratio is $\mu = 0.1$, and the groove depth is (a) $h = 2$ (corresponding to grooves of square cross section) and (b) $h = 1/2$. (c) Resulting slip length λ as function of μ, for various values of h.

III. SHALLOW GROOVES

We begin by briefly considering the limit of shallow grooves, $h \ll 1$. It is readily seen that the one-dimensional linear profiles

$$w^{+} = y + \frac{h}{\mu}, \qquad w^{-} = \frac{y + h}{\mu}, \tag{3.1a,b}$$

satisfy the governing equations (2.1)–(2.7), except for the no-slip conditions (2.4a) and (2.7) on the ridge. This suggests that Eqs. (3.1) should be interpreted asymptotically as leading-order "outer" approximations in the limit $h \ll 1$ with y/h fixed [33], which break down near the ridge. Definition (2.8) then yields the slip length

$$\lambda \approx \frac{h}{\mu}, \tag{3.2}$$

which is small (as long as $h \ll \mu$). This is to be expected, as the flow of the lubricant is resisted by the bottom boundary.

While the lubrication-type approximation (3.2) is simple and intuitive, we will see that its validity for small μ is severely limited.

IV. LOCAL ANALYSIS NEAR THE RIDGE TIP

We next analyze the local structure of the velocity field in the vicinity of the ridge tip, $(x, y) = (0, 0)$. We start by reformulating the relevant governing equations in terms of polar coordinates (ρ, ϕ) centered about the tip, defined [see Fig. 1(c)] via $(x, y) = (\rho\cos\phi, \rho\sin\phi)$. These governing equations include Laplace's equation in the exterior and interior domains [cf. Eq. (2.1)],

$$\rho\frac{\partial}{\partial\rho}\left(\rho\frac{\partial w^{\pm}}{\partial\rho}\right)+\frac{\partial^2 w^{\pm}}{\partial\phi^2}=0 \quad \text{for} \quad 0<\pm\phi<\frac{\pi}{2}; \tag{4.1}$$

the conditions of continuous velocity and shear stress [cf. Eq. (2.2)],

$$w^{+}=w^{-} \quad \text{at} \quad \phi=0, \qquad \frac{\partial w^{+}}{\partial\phi}=\mu\frac{\partial w^{-}}{\partial\phi} \quad \text{at} \quad \phi=0; \tag{4.2a,b}$$

the requirements at $x = 0$ for no slip on the ridge and symmetry in the exterior domain [cf. Eqs. (2.4a) and (2.5a)],

$$w^{-}=0 \quad \text{at} \quad \phi=-\frac{\pi}{2}, \qquad \frac{\partial w^{+}}{\partial\phi}=0 \quad \text{at} \quad \phi=\frac{\pi}{2}; \tag{4.3a,b}$$

and the tip condition [cf. Eq. (2.7)],

$$\lim_{\rho\to 0} w^{+}=0. \tag{4.4}$$

The remaining conditions [Eqs. (2.3), (2.4b), (2.5b) and (2.6)] do not affect the local analysis as they apply away from the tip.

We now seek a leading-order local approximation of the velocity field as $\rho \searrow 0$. We denote this approximation by $w_L^{\pm}(\rho, \phi)$ and assume that it is a power law in ρ, i.e., proportional to ρ^{α}, where the unknown exponent α is positive in order to satisfy Eq. (4.4). The general power-law solution of Eq. (4.1) is of the form

$$w_L^{\pm}(\rho,\phi)=\rho^{\alpha}[A^{\pm}\cos(\alpha\phi)+B^{\pm}\sin(\alpha\phi)]. \tag{4.5}$$

Continuity of velocity, Eq. (4.2a), demands $A^{+} = A^{-}$; we denote this common value by A. Continuity of shear stress, Eq. (4.2b), and the no-slip and symmetry conditions, Eqs. (4.3), yield the relations

$$B^{+}=\mu B^{-}, \quad A\cos\frac{\alpha\pi}{2}-B^{-}\sin\frac{\alpha\pi}{2}=0, \quad -A\sin\frac{\alpha\pi}{2}+B^{+}\cos\frac{\alpha\pi}{2}=0. \tag{4.6}$$

Upon eliminating $B^{\pm}$, we obtain the condition $\tan(\alpha\pi/2) = \pm\mu^{1/2}$ determining the allowed values of α. The dominant local behavior is given by the smallest (positive) value,

$$\alpha=\frac{2}{\pi}\arctan\mu^{1/2}. \tag{4.7}$$

The associated solution is

$$w_L^{+}=A\rho^{\alpha}[\cos(\alpha\phi)+\mu^{1/2}\sin(\alpha\phi)], \qquad w_L^{-}=A\rho^{\alpha}[\cos(\alpha\phi)+\mu^{-1/2}\sin(\alpha\phi)]. \tag{4.8a,b}$$

The constant A is an overall amplitude that is determined by global considerations.

We conclude that, at the interface $y = 0$, the leading-order local behavior of the velocity and shear stress are given by

$$w_L^{+}=w_L^{-}=Ax^{\alpha}, \qquad \frac{\partial w_L^{+}}{\partial y}=\mu\frac{\partial w_L^{-}}{\partial y}=A\alpha\mu^{1/2}x^{\alpha-1}. \tag{4.9a,b}$$

This local solution suggests that the contribution to the drag integral [Eqs. (2.10)] from some small region $0 < x < \delta$, where $\delta \ll 1$, can be approximated as

$$\mu\int_0^{\delta}\left.\frac{\partial w^{-}}{\partial y}\right|_{y=0}dx\approx A\mu^{1/2}\delta^{\alpha}. \tag{4.10}$$

Later, we will employ this estimate for scaling purposes.

V. NEARLY INVISCID LUBRICANT

We now consider the limit

$$\mu \ll 1, \tag{5.1}$$

where we anticipate that the slip length is asymptotically large.

A. Scaling arguments based on local analysis

While the local analysis of Sec. IV has been derived in the limit $\rho \to 0$ for fixed μ, it turns out that expanding its results for $\mu \ll 1$ can give some intuition for the behavior of the solution near the tip when μ is small. For small μ, we find that the exponent α of the local behavior, given by Eq. (4.7), is approximately

$$\alpha \approx \frac{2\mu^{1/2}}{\pi}, \tag{5.2}$$

which is also small. Provided $\alpha \ln \rho$ is small, we can then approximate

$$\rho^{\alpha} \approx 1 + \mu^{1/2}\frac{2}{\pi}\ln\rho. \tag{5.3}$$

Thus, the leading-order local approximations (4.8) simplify to

$$w^{+} \approx A\left(1 + \mu^{1/2}\frac{2}{\pi}\ln\rho\right), \qquad w^{-} \approx A\left(1 + \frac{2\phi}{\pi}\right)\left(1 + \mu^{1/2}\frac{2}{\pi}\ln\rho\right). \tag{5.4a,b}$$

We first note that the approximations (5.4) explain the near-tip behavior seen in Figs. 2(a) and 2(b). In the exterior domain ($y > 0$), the contours are quarter-circular due to the independence upon ϕ, but in the interior domain ($y < 0$), the contours are radial due to the leading-order independence upon ρ.

Second, the estimate (4.10) for the contribution to the drag integral [Eqs. (2.10)] from a small region near the tip, using the small-μ approximation (5.2), becomes

$$\mu\int_0^{\delta}\left.\frac{\partial w^{-}}{\partial y}\right|_{y=0} dx \approx A\mu^{1/2} \tag{5.5}$$

(provided that $\mu^{1/2}\ln\delta$ is small). Assuming that this forms a non-negligible part of the total drag, Eq. (2.12) suggests that $A = \mathrm{ord}(\mu^{-1/2})$. [In fact, it will turn out that (5.5) is the sole contribution to the drag integral at ord(1), so that the force balance (2.13b) gives $A \sim \mu^{-1/2}$.]

B. Asymptotic structure for nearly inviscid lubricant

For $\mu \ll 1$, the intuitive arguments in Sec. V A suggest that velocities should be $\mathrm{ord}(\mu^{-1/2})$ in order to result in an ord(1) drag. We therefore postulate the expansions

$$w^{\pm} \sim \mu^{-1/2}w^{\pm}_{-1}(x,y) + w^{\pm}_{0}(x,y) + \mu^{1/2}w^{\pm}_{1}(x,y) + \cdots, \tag{5.6}$$

$$\lambda \sim \mu^{-1/2}\lambda_{-1} + \lambda_0 + \mu^{1/2}\lambda_1 + \cdots, \tag{5.7}$$

as $\mu \to 0$. The far-field condition (2.9) then yields

$$w^{+}_{-1} \sim \lambda_{-1}, \qquad w^{+}_{0} \sim y + \lambda_0, \tag{5.8a,b}$$

as $y \to \infty$, and continuity of shear stress [Eq. (2.2b)] yields

$$\frac{\partial w^{+}_{-1}}{\partial y} = 0, \qquad \frac{\partial w^{+}_{0}}{\partial y} = 0, \qquad \frac{\partial w^{+}_{1}}{\partial y} = \frac{\partial w^{-}_{-1}}{\partial y}, \tag{5.9a,b,c}$$

at $y = 0$. The remainder of Eqs. (2.1)–(2.7) simply retain their homogeneous form at each order.

It may appear from Eqs. (5.9a), (5.9b), and (2.10) that the drag $\mathcal{D}$ is $O(\mu^{1/2})$, seemingly too small to satisfy Eq. (2.12). The resolution to this apparent contradiction is that the expansions (5.6) represent an *outer* asymptotic region where $(x, y) = \mathrm{ord}(1)$, whereas the dominant force is provided by an *inner* asymptotic region about the tip of the ridge, $(x, y) = (0, 0)$. (The scaling of the thickness of this inner region will be determined later.) The no-slip condition at the tip, Eq. (2.7), is accordingly omitted from the outer problems posed above, as it rather applies to the inner region. Similarly, the shear-stress continuity conditions (5.9) are henceforth understood to hold for $x > 0$.

An alternative (and perhaps more tempting) resolution would be to assume that the velocities and slip length are $\mathrm{ord}(\mu^{-1})$ instead, to directly yield an $\mathrm{ord}(1)$ shear stress at the interface. However, following such a calculation through, or appealing to Eq. (5.5), would reveal an $\mathrm{ord}(\mu^{-1/2})$ contribution from near the tip to the drag integral [Eqs. (2.10)], in contradiction to Eq. (2.12). Attempting any other large scaling for $w^{\pm}$ and λ similarly results in a viscous drag of the wrong order; only the scaling (5.6) and (5.7) yields a self-consistent result.

We now proceed to calculate the leading-order slip length λ_{-1} by considering the outer approximation in the exterior domain, the inner approximation in both the exterior and interior domains, and the force balances (2.13).

C. Outer approximation in the exterior domain

We first consider the leading-order outer flow in the exterior domain, w^{+}_{-1}. It is governed by Laplace's equation (2.1) together with the lateral symmetry conditions (2.5), the far-field streaming condition (5.8a), and the shear-free interface condition (5.9a). This outer problem suggests the uniform flow

$$w^{+}_{-1} \equiv \lambda_{-1}. \tag{5.10}$$

The leading-order outer approximation (5.10) fails to satisfy no slip at the ridge tip; this, of course, is in accordance with the supposed existence of the inner region. In order to identify the scaling of that region, it is helpful to briefly consider the outer correction w^{+}_{0}—in particular, its behavior as $\rho \to 0$. (A detailed analysis of w^{+}_{0} will be carried out in Sec. VI.)

At $\mathrm{ord}(1)$, the generalized drag expression (2.14) gives, using (2.12),

$$\int_0^1 \frac{\partial w^{+}_{0}}{\partial y}\, dx = 1. \tag{5.11}$$

While the exact expression (2.14) holds for all $y \geqslant 0$, it only implies Eq. (5.11) for $y > 0$, since the outer expansion (5.6) fails at the origin $(x, y) = (0, 0)$. The ambiguity of Eq. (5.11) at $y = 0$, in conjunction with the integral apparently vanishing there owing to the shear-free condition (5.9b), suggests that w^{+}_{0} has a singularity at the origin.

To characterize the singularity, we employ the generalized force balance (2.13c) at $\mathrm{ord}(1)$,

$$\int_{\mathcal{C}} \hat{\mathbf{n}} \cdot \nabla w^{+}_{0}\, dl = 1, \tag{5.12}$$

with $\mathcal{C}$ the union of a quarter-circle of radius $0 < \delta < 1$ centered at the origin (within the exterior semiunit cell) and the interval $x \in (\delta, 1)$ on $y = 0$. Given the stress-free interface condition (5.9b), only the quarter-circle has a nonzero contribution. By letting $\delta \to 0$, we see that the total force emanating from this "corner" is 1. We therefore expect the singularity to be a source of strength 4, i.e.,

$$w^{+}_{0} \sim \frac{2}{\pi} \ln \rho \quad \text{as} \quad \rho \to 0. \tag{5.13}$$

In principle, this asymptotic behavior could include more singular terms (without modifying the net force); these, however, can be ruled out via matching considerations.

D. Inner tip region

To determine the scaling of the inner region near the tip, we consider the local behavior as $\rho \to 0$ of the first two terms in the expansion (5.6) for w^+. Equations (5.10) and (5.13) show that the expansion breaks down once the exponentially small scale set by $\ln(1/\rho) = \mathrm{ord}(\mu^{-1/2})$ is reached; on that scale, the second term becomes asymptotically comparable to the first.

This observation suggests that an appropriate rescaled coordinate σ for the inner region near the tip is given by

$$\sigma = \mu^{1/2} \ln \rho. \tag{5.14}$$

The coordinate σ is negative, with the tip $\rho = 0$ located at $\sigma = -\infty$. Matching to the outer region $\rho = \mathrm{ord}(1)$ takes place for small σ, specifically on the intermediate scale $\mu^{1/2} \ll \sigma \ll 1$.

We define the tip-scale velocity fields $\omega^{\pm}(\sigma, \phi) = w^{\pm}(\rho, \phi)$. They satisfy the following equations [cf. Eqs. (4.1)–(4.4) in the local analysis]:

$$\frac{\partial^2 \omega^{\pm}}{\partial \phi^2} + \mu \frac{\partial^2 \omega^{\pm}}{\partial \sigma^2} = 0 \quad \text{for} \quad 0 < \pm\phi < \frac{\pi}{2}, \tag{5.15}$$

$$\omega^+ = \omega^- \quad \text{at} \quad \phi = 0, \qquad \frac{\partial \omega^+}{\partial \phi} = \mu \frac{\partial \omega^-}{\partial \phi} \quad \text{at} \quad \phi = 0, \tag{5.16a,b}$$

$$\omega^- = 0 \quad \text{at} \quad \phi = -\frac{\pi}{2}, \qquad \frac{\partial \omega^+}{\partial \phi} = 0 \quad \text{at} \quad \phi = \frac{\pi}{2}, \tag{5.17a,b}$$

$$\lim_{\sigma \to -\infty} \omega^+ = 0. \tag{5.18}$$

We accordingly posit the inner expansions

$$\omega^{\pm}(\sigma, \phi) \sim \mu^{-1/2} \omega^{\pm}_{-1}(\sigma, \phi) + \omega^{\pm}_0(\sigma, \phi) + \mu^{1/2} \omega^{\pm}_1(\sigma, \phi) + \cdots \quad \text{as} \quad \mu \to 0, \tag{5.19}$$

and seek to calculate $\omega^{\pm}_{-1}$. The set of homogeneous equations (5.15)–(5.18) is supplemented at each order with the requirement of matching to the outer region. In particular, at leading order, the uniform solution (5.10) implies the inhomogeneous matching condition

$$\lim_{\sigma \to 0} \omega^+_{-1} = \lambda_{-1}. \tag{5.20}$$

We start with the exterior domain. It is easy to see from the governing equation (5.15) with the symmetry condition (5.17b) at $\mathrm{ord}(\mu^{-1/2})$ that ω^+_{-1} cannot depend upon ϕ:

$$\omega^+_{-1} = \omega^+_{-1}(\sigma). \tag{5.21}$$

Thus, the governing equation (5.15) at $\mathrm{ord}(\mu^{1/2})$ becomes

$$\frac{\partial^2 \omega^+_1}{\partial \phi^2} = -\frac{d^2 \omega^+_{-1}}{d\sigma^2}. \tag{5.22}$$

Integrating this over $0 \leqslant \phi \leqslant \pi/2$ and using the symmetry condition (5.17b) yields

$$\frac{\partial \omega^+_1}{\partial \phi} = \frac{\pi}{2} \frac{d^2 \omega^+_{-1}}{d\sigma^2} \quad \text{at} \quad \phi = 0. \tag{5.23}$$

Consider now the interior domain at $\mathrm{ord}(\mu^{-1/2})$. Solving the governing equation (5.15) with the no-slip condition (5.17a) and continuity condition (5.16a) gives

$$\omega^-_{-1}(\sigma, \phi) = \left(1 + \frac{2\phi}{\pi}\right) \omega^+_{-1}(\sigma). \tag{5.24}$$

Substitution of Eqs. (5.23) and (5.24) into the shear-stress condition (5.16b) at ord($\mu^{1/2}$) then gives an ordinary differential equation for ω_{-1}^{+},

$$\frac{d^2\omega_{-1}^{+}}{d\sigma^2} = \frac{4}{\pi^2}\omega_{-1}^{+}. \tag{5.25}$$

The solution that satisfies the tip condition (5.18) and matching condition (5.20) is

$$\omega_{-1}^{+} = \lambda_{-1}e^{2\sigma/\pi}. \tag{5.26a}$$

The corresponding leading-order interior solution (5.24) is

$$\omega_{-1}^{-} = \lambda_{-1}\left(1 + \frac{2\phi}{\pi}\right)e^{2\sigma/\pi}. \tag{5.26b}$$

Reassuringly, the form of the inner solutions (5.26) agrees with the small-μ expansion [Eqs. (5.4)] of the results from the local analysis.

E. Leading-order drag and slip length

It remains to determine the slip length λ_{-1}. We turn to the viscous-drag integral (2.13b), and split it into separate contributions from the tip and outer regions, $\mathcal{D} = \mathcal{D}_{\text{tip}} + \mathcal{D}_{\text{outer}}$, where

$$\mathcal{D}_{\text{tip}} = \mu\int_0^{\delta}\left.\frac{\partial w^{-}}{\partial y}\right|_{y=0} dx, \qquad \mathcal{D}_{\text{outer}} = \mu\int_{\delta}^{1}\left.\frac{\partial w^{-}}{\partial y}\right|_{y=0} dx. \tag{5.27a,b}$$

By virtue of the force balance (2.13b),

$$\mathcal{D}_{\text{tip}} + \mathcal{D}_{\text{outer}} = 1. \tag{5.27c}$$

The splitting point $x = \delta$ is chosen to be on an "intermediate" scale between the outer scale $x =$ ord(1) and the inner scale $\sigma =$ ord(1) [see Eq. (5.14)]. This intermediate scale is represented by the conditions

$$\delta \ll 1, \qquad \ln\frac{1}{\delta} \ll \mu^{-1/2}. \tag{5.28a,b}$$

Since the outer solution is ord($\mu^{-1/2}$) [cf. Eq. (5.6)], the outer contribution $\mathcal{D}_{\text{outer}}$ scales as $\mu^{1/2}$ and does not contribute at leading order to Eq. (5.27c).

For the tip contribution, we transform via polar coordinates (ρ, ϕ) into tip coordinates (σ, ϕ) using Eq. (5.14), and obtain

$$\mathcal{D}_{\text{tip}} = \mu^{1/2}\int_{-\infty}^{-\mu^{1/2}\ln(1/\delta)}\left.\frac{\partial\omega^{-}}{\partial\phi}\right|_{\phi=0} d\sigma. \tag{5.29}$$

Using the leading-order tip solution (5.26b) and replacing the upper integration limit with 0 [due to Eq. (5.28b)], we obtain the result

$$\mathcal{D}_{\text{tip}} \sim \frac{2\lambda_{-1}}{\pi}\int_{-\infty}^{0} e^{2\sigma/\pi}\, d\sigma = \lambda_{-1}. \tag{5.30}$$

We conclude from the force balance (5.27c) that the leading-order slip length is simply given by

$$\lambda_{-1} = 1, \tag{5.31}$$

that is,

$$\lambda \sim \mu^{-1/2} \quad \text{for} \quad \mu \ll 1. \tag{5.32}$$

[An alternative derivation makes use of van Dyke matching [35]: Writing Eq. (5.26a) for ω_{-1}^{+} in terms of the outer coordinate ρ and expanding for $\mu \ll 1$ gives

$$\mu^{-1/2}\lambda_{-1} + \frac{2\lambda_{-1}}{\pi} \ln \rho + \cdots . \tag{5.33}$$

Comparison with Eq. (5.13) then yields the result (5.31).]

The leading-order results for $\mu \ll 1$ can be summarized as follows. The velocity in the exterior domain $y > 0$ is approximately uniform, $w^{+} \approx \lambda$ [see Eq. (5.10)]. Given the need to satisfy the no-slip condition, this uniform "slip flow" is disturbed in an exponentially small inner region about the tip [see Eqs. (5.26)]. This disturbance, in turn, results in a viscous drag $\approx \mu^{1/2}\lambda$. Other contributions to the drag only enter at higher order, so the balance (2.13a) between the viscous drag and the unity-imposed shear yields the result $\lambda \approx \mu^{-1/2}$ [see Eq. (5.32)].

VI. FIRST CORRECTION TO SLIP LENGTH

In the previous section, we determined the first term in the expansion

$$\lambda \sim \mu^{-1/2} + \lambda_0 \quad \text{for} \quad \mu \ll 1. \tag{6.1}$$

We proceed here to determine the correction, λ_0, which depends upon the groove depth h. This involves calculating the first corrections (smaller by an order $\mu^{1/2}$) to the outer approximation in the exterior domain and the inner (tip) approximation in both domains, as well as a leading-order outer approximation in the interior domain. We subsequently use these results to extend approximation (5.30) for $\mathcal{D}_{\text{tip}}$ to a higher order, and to calculate the leading-order contribution to $\mathcal{D}_{\text{outer}}$ from the interior solution.

A. First correction to the outer approximation in the exterior domain

We begin with the asymptotic correction w_0^{+} to the uniform leading-order outer approximation in the exterior domain, Eq. (5.10). To aid the calculation, we introduce a shifted field,

$$\tilde{w}_0^{+} = w_0^{+} - \lambda_0, \tag{6.2}$$

so that λ_0 is eliminated from the far-field condition (5.8b):

$$\tilde{w}_0^{+} = y + o(1) \quad \text{as} \quad y \to \infty. \tag{6.3}$$

The problem governing $\tilde{w}_0^{+}$ is given by Laplace's equation [recall Eq. (2.1)]; homogeneous Neumann conditions at $x = 0$, $x = 1$, and $y = 0$, excluding the origin [cf. Eqs. (2.5) and (5.9b)]; the far-field condition (6.3); and Eq. (5.13), which follows from matching to the tip region [see Eq. (5.33)]. Hence, $\tilde{w}_0^{+}$ has a unique solution that is *universal*; i.e., it does not depend on any parameters. In particular, it follows from the local behavior (5.13) that we can define the pure number

$$\beta = \lim_{\rho \to 0} \left(\tilde{w}_0^{+} - \frac{2}{\pi} \ln \rho \right), \tag{6.4}$$

and deduce that

$$w_0^{+} \sim \frac{2}{\pi} \ln \rho + \lambda_0 + \beta \quad \text{as} \quad \rho \to 0. \tag{6.5}$$

Expression (6.5) needs to match the inner region at the next order.

The universal problem possesses the explicit solution (see Appendix B)

$$\tilde{w}_0^{+} = \frac{1}{\pi} \ln \left[4 \left(\sin^2 \frac{\pi x}{2} + \sinh^2 \frac{\pi y}{2} \right) \right], \tag{6.6}$$

whereby Eq. (6.4) gives

$$\beta = \frac{2}{\pi}\ln\pi. \tag{6.7}$$

B. First corrections to the inner tip approximations

Continuing to the tip region, we observe that the analysis in Sec. V D can be repeated at one higher order, to yield

$$\omega_0^+ = C_0 e^{2\sigma/\pi}, \qquad \omega_0^- = C_0\left(1+\frac{2\phi}{\pi}\right)e^{2\sigma/\pi}. \tag{6.8a,b}$$

The constant C_0 is determined by 2-2 van Dyke matching [35] to the outer exterior solution, as follows. Taking the inner field ω^+ up to ord(1) [i.e., Eqs. (5.26a) and (6.8a), making use of Eq. (5.31)], rewriting in terms of the outer coordinate ρ, and expanding for small μ gives, when retaining terms up to ord(1),

$$\mu^{-1/2} + \frac{2}{\pi}\ln\rho + C_0. \tag{6.9}$$

Comparing with the outer behavior [i.e., Eqs. (5.10) and (6.5)], we conclude that $C_0 = \beta + \lambda_0$, and hence Eqs. (6.8) become

$$\omega_0^+ = (\beta+\lambda_0)e^{2\sigma/\pi}, \qquad \omega_0^- = (\beta+\lambda_0)\left(1+\frac{2\phi}{\pi}\right)e^{2\sigma/\pi}. \tag{6.10a,b}$$

To complete the calculation and determine λ_0, we need to revisit the viscous-drag integrals (5.27).

C. Corrections to the viscous drag

We first evaluate the tip contribution $\mathcal{D}_{\rm tip}$ in (5.27a) to ord($\mu^{1/2}$) using the first two terms in the expansion (5.19). The leading-order approximation (5.26b) contributes, using Eq. (5.31),

$$\int_{-\infty}^{\mu^{1/2}\ln\delta} \frac{2}{\pi}e^{2\sigma/\pi}\,d\sigma \sim 1 + \mu^{1/2}\frac{2}{\pi}\ln\delta, \tag{6.11}$$

where we again exploit the fact that $\mu^{1/2}\ln\delta \ll 1$ [see Eqs. (5.28)]. Similarly, the correction (6.10b) contributes

$$\mu^{1/2}\int_{-\infty}^{\mu^{1/2}\ln\delta}(\beta+\lambda_0)\frac{2}{\pi}e^{2\sigma/\pi}\,d\sigma \sim \mu^{1/2}(\beta+\lambda_0). \tag{6.12}$$

Hence, the tip contribution is

$$\mathcal{D}_{\rm tip} \sim 1 + \mu^{1/2}\left(-\frac{2}{\pi}\ln\frac{1}{\delta} + \beta + \lambda_0\right). \tag{6.13}$$

The outer contribution $\mathcal{D}_{\rm outer}$ in Eq. (5.27b) depends on the leading-order outer approximation in the interior domain, w_{-1}^-. Prior to calculating w_{-1}^-, we derive expressions for $\mathcal{D}_{\rm outer}$ and the correction λ_0 in terms of integral properties of that field.

Given that w_{-1}^- matches to the tip solution ω_{-1}^- [given by Eqs. (5.26b) and (5.31)], we can deduce its local behavior:

$$w_{-1}^- \sim 1 + \frac{2\phi}{\pi} \quad \text{as} \quad \rho \to 0. \tag{6.14}$$

Consequently, the shear at the interface has the near-tip behavior

$$\left.\frac{\partial w_{-1}^-}{\partial y}\right|_{y=0} \sim \frac{2}{\pi x} \quad \text{as} \quad x \to 0, \tag{6.15}$$

which results in a logarithmic divergence in the drag integral (5.27b) as $\delta \to 0$. We subtract off this singularity from the integral to obtain

$$\mathcal{D}_{\text{outer}} \sim \mu^{1/2}\left[\int_\delta^1 \left(\left.\frac{\partial w_{-1}^-}{\partial y}\right|_{y=0} - \frac{2}{\pi x}\right) dx - \frac{2}{\pi}\ln\delta\right]. \tag{6.16}$$

This motivates defining a "regularized" drag contribution

$$\mathcal{F}(h) = \int_0^1 \left(\left.\frac{\partial w_{-1}^-}{\partial y}\right|_{y=0} - \frac{2}{\pi x}\right) dx, \tag{6.17}$$

where we make it explicit that $\mathcal{F}$ depends only on the groove depth h. Equation (6.16) then simplifies to

$$\mathcal{D}_{\text{outer}} \sim \mu^{1/2}\left[\mathcal{F}(h) + \frac{2}{\pi}\ln\frac{1}{\delta}\right]. \tag{6.18}$$

Upon substitution of the drag contributions (6.13) and (6.18) into the force balance (5.27c), the terms involving $\ln\delta$ cancel out, as they should, and the remaining terms at ord($\mu^{1/2}$) determine the correction to the slip length,

$$\lambda_0 = -\mathcal{F}(h) - \beta, \tag{6.19}$$

where β is given by Eq. (6.7).

D. Leading-order outer approximation in the interior domain

At this stage all that remains is to calculate the leading-order outer approximation in the interior domain, w_{-1}^-, and use Eqs. (6.17) and (6.19) to calculate λ_0.

The field w_{-1}^- satisfies Laplace's equation [cf. Eq. (2.1)], no-slip conditions at $x = 0$ and $y = -h$ [cf. Eqs. (2.4)], and the symmetry condition (2.3) at $x = 1$. The flow is driven by the leading-order uniform exterior flow $w_{-1}^+ \equiv 1$ [cf. Eqs. (5.10) and (5.31)] via continuity of velocity at the interface (2.2a), which yields

$$w_{-1}^- = 1 \quad \text{at} \quad y = 0. \tag{6.20}$$

The field w_{-1}^- must also satisfy a matching condition to the inner solution (5.26b) near the origin. A local analysis near the origin reveals, however, that this condition is trivially satisfied provided w_{-1}^- remains bounded. We thus have a well-posed problem governing w_{-1}^- for all values of the depth h.

We first consider the limiting case of infinitely deep grooves, $h = \infty$, for which the no-slip condition at $y = -h$ is replaced by the decay condition

$$\lim_{y\to-\infty} w_{-1}^- = 0. \tag{6.21}$$

The associated calculation of w_{-1}^- is carried out in Appendix C 1. It results in

$$\left.\frac{\partial w_{-1}^-}{\partial y}\right|_{y=0} = \frac{1}{\sin(\pi x/2)}, \tag{6.22}$$

which indeed blows up as $x \to 0$ according to Eq. (6.15). Substitution of Eq. (6.22) into Eq. (6.17) yields

$$\mathcal{F}(\infty) = \frac{2}{\pi}\ln\frac{4}{\pi}, \tag{6.23}$$

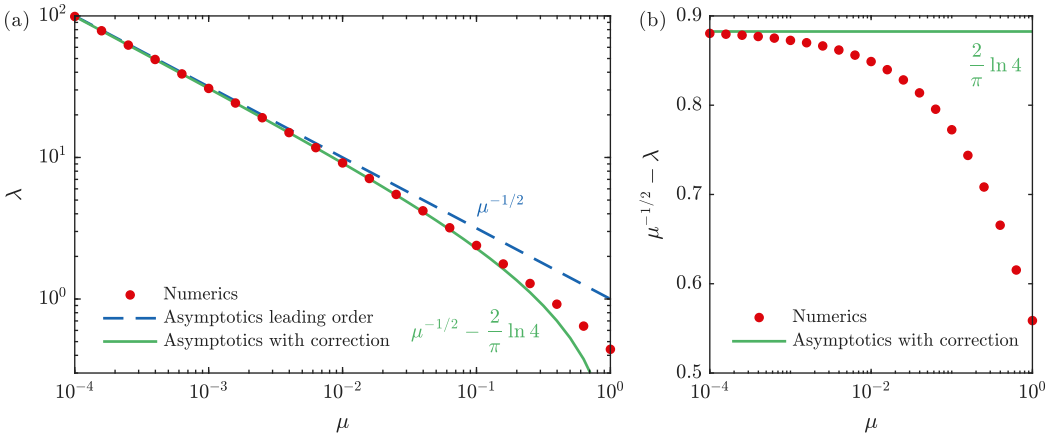


FIG. 3. (a) Slip length λ as a function of viscosity ratio μ for deep grooves ($h = \infty$), comparing (symbols) numerical results with (dashed curve) the leading-order approximation (5.32) and (solid curve) the two-term approximation (6.25). (b) Deviation from the leading-order asymptotic prediction, comparing numerical results and the asymptotic prediction $-\lambda_0$ obtained from Eq. (6.24).

whereby, from Eq. (6.19),

$$\lim_{h\to\infty} \lambda_0 = -\frac{2}{\pi}\ln 4. \tag{6.24}$$

Thus, for $h = \infty$, Eq. (5.32) is refined to

$$\lambda \sim \mu^{-1/2} - \frac{2}{\pi}\ln 4 \quad \text{for} \quad \mu \ll 1. \tag{6.25}$$

In Fig. 3(a), we compare the leading-order approximation (5.32) and two-term approximation (6.25) with the slip length λ calculated using the numerical scheme. Figure 3(b) shows the variation with μ of the difference $\mu^{-1/2} - \lambda$; it is evident that this difference indeed approaches Eq. (6.24).

Another limit of interest is that of shallow grooves, $h \ll 1$. Here the approximate solution $w_{-1}^- \sim 1 + y/h$ [analogous to Eq. (3.1b)] is readily obtained by disregarding the no-slip ridge condition (2.4a). At leading order in h we then find, from Eqs. (6.17) and (6.19),

$$\lambda_0 \sim -\frac{1}{h} \quad \text{for} \quad h \ll 1. \tag{6.26}$$

In principle, asymptotic corrections to Eqs. (6.24) and (6.26) could be derived by perturbative analyses of the interior problem governing w_{-1}^-. In particular, the correction to the shallow-grooves approximation (6.26) could be obtained by analyzing the end region near $x = 0$ [36,37] and its contribution to the integral (6.17). It turns out, however, that the problem governing w_{-1}^- for arbitrary h can be solved exactly.

The solution is derived in Appendix C 2 using a Schwarz-Christoffel mapping. It results in the regularized shear force

$$\mathcal{F}(h) = \frac{2}{\pi}\ln\frac{2}{\sqrt{1-k^2}\,\mathrm{K}(k^2)}, \tag{6.27}$$

where K is the complete elliptic integral of the first kind and k is given by the implicit relation

$$\frac{\mathrm{K}(1-k^2)}{\mathrm{K}(k^2)} = h. \tag{6.28}$$

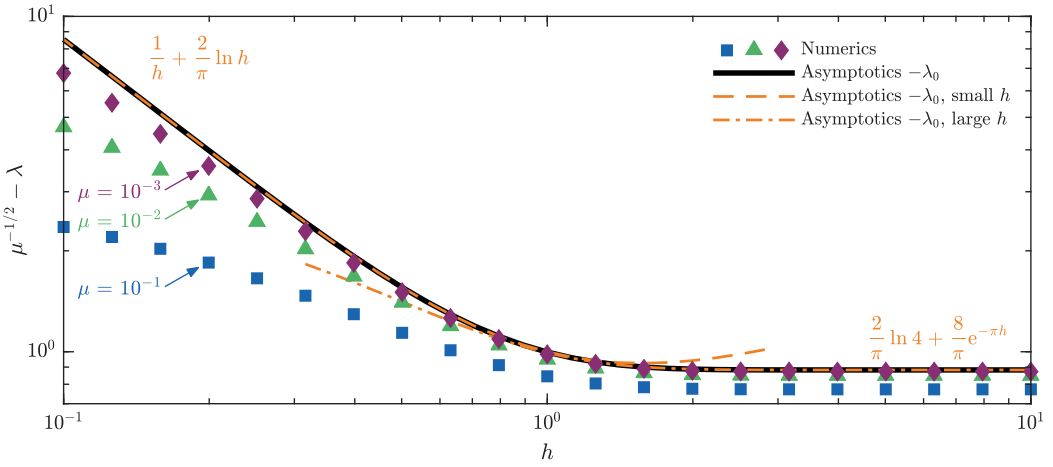


FIG. 4. Variation with groove depth h of $\mu^{-1/2} - \lambda$, the (negative of the) slip-length deviation from the leading-order asymptotic prediction (cf. Fig. 3). The symbols show numerical results for three values of the viscosity ratio μ. The curves show asymptotic results for $-\lambda_0$: solid curve, exact result [Eq. (6.29)]; dashed curve, small-h approximation [Eq. (6.32)]; and dash-dotted curve, large-h approximation [Eq. (6.31)].

[We employ the convention where the argument m of $\mathrm{K}(m)$ is the "parameter"—the square of the "modulus."] Substitution of Eq. (6.27) into Eq. (6.19) finally yields

$$\lambda_0 = \frac{2}{\pi} \ln \frac{\sqrt{1-k^2}\,\mathrm{K}(k^2)}{2\pi}, \tag{6.29}$$

and hence the two-term approximation for the slip length, valid for arbitrary (fixed) $h > 0$, is

$$\lambda \sim \mu^{-1/2} + \frac{2}{\pi} \ln \frac{\sqrt{1-k^2}\,\mathrm{K}(k^2)}{2\pi} \quad \text{as} \quad \mu \to 0, \tag{6.30}$$

where k depends on h via Eq. (6.28).

Revisiting the limits of deep and shallow grooves, we can expand Eq. (6.29) using the asymptotic behavior of the elliptic integral [38]. For deep grooves, where $k \searrow 0$, we obtain

$$\lambda_0 = -\frac{2}{\pi} \ln 4 - \frac{8}{\pi} e^{-\pi h} + O(e^{-2\pi h}) \quad \text{for} \quad h \gg 1, \tag{6.31}$$

which provides a refinement of approximation (6.24). For shallow grooves, where $k \nearrow 1$, we obtain

$$\lambda_0 = -\frac{1}{h} + \frac{2}{\pi} \ln \frac{1}{h} + O(e^{-\pi/h}) \quad \text{for} \quad h \ll 1, \tag{6.32}$$

which provides a refinement of approximation (6.26).

The variation with h of $-\lambda_0$ is shown in Fig. 4. Unsurprisingly, the agreement between the asymptotic and numerical results improves as μ diminishes. We note, however, that the asymptotic scheme fails as h becomes small, even for small values of μ. This failure motivates a careful look at the scenario where *both* μ and h are small.

VII. SHALLOW GROOVES: DISTINGUISHED LIMIT AND SLIP LENGTH

According to Eq. (6.32), the correction λ_0 in the slip-length expansion (6.1) grows in magnitude as h decreases. Hence, the expansion breaks down for h on the order of $\mu^{1/2}$, when the correction becomes comparable to the leading-order term. Indeed, a breakdown for sufficiently small h may be anticipated given the need to transition to the shallow-groove approximation (3.2).

A leading-order approximation describing that transition can be derived intuitively following arguments analogous to those employed at the end of Sec. V E. As before, the leading-order uniform exterior solution $w^+ \approx \lambda$ [cf. Eq. (5.10)] drives shear near the tip, which contributes a drag $\mathcal{D}_{\text{tip}} \approx \mu^{1/2}\lambda$ to the force integral (5.27) [see Eq. (5.30)]. The exterior solution also drives flow in the interior fluid, which due to the shallow geometry is approximately $w^- \approx \lambda(1 + y/h)$ [cf. Eq. (3.1b)]. This contributes a drag $\mathcal{D}_{\text{outer}} \approx \mu\lambda/h$, which for h small as $\mu^{1/2}$ becomes comparable to $\mathcal{D}_{\text{tip}}$. Since the total drag adds up to unity [see Eq. (5.27c)], we can solve for λ to obtain the result

$$\lambda \approx \frac{1}{\mu^{1/2} + \mu/h} \quad \text{for } \mu \ll 1, \tag{7.1}$$

with the two terms in the denominator being comparable for h on the order of $\mu^{1/2}$. If $h \gg \mu^{1/2}$, $\mathcal{D}_{\text{outer}}$ is negligible and we recover the main result (5.32); if $h \ll \mu^{1/2}$, $\mathcal{D}_{\text{tip}}$ is negligible and we recover the shallow-groove result (3.2).

In what follows, we proceed to formalize the intuitive calculation leading to Eq. (7.1), making use of the distinguished limit

$$\mu, h \to 0 \quad \text{with} \quad H = h/\mu^{1/2} \text{ fixed}. \tag{7.2}$$

This is followed by the calculation of the next-order correction to obtain a two-term approximation to the slip length, analogous to Eq. (6.30).

A. Asymptotic regions and problem formulation

Since the depth h is ord$(\mu^{1/2})$, and the two terms in Laplace's equation (2.1) balance when x and y are of comparable size, we anticipate the emergence of an intermediate asymptotic region, of ord$(\mu^{1/2})$ extent, about the ridge. This is also hinted at by the results shown in Fig. 2(b): in the shallow interior domain, the variation is predominantly in the y direction (as seen in the form of nearly horizontal contours), except within a distance of order h about the ridge, representing the intermediate region.

We thus introduce the stretched intermediate coordinates

$$(X, Y) = \frac{(x, y)}{\mu^{1/2}}, \tag{7.3}$$

for which the bottom boundary $y = -h$ becomes $Y = -H$. We continue to use $w^+(x, y)$ to denote the velocity in the exterior outer domain. Since the interior outer domain is shallow, we denote (with a slight abuse of notation) the velocity field there by $w^-(x, Y)$. For the intermediate region, we introduce the notation $W^{\pm}(X, Y)$, and for the exponentially small tip regions, we continue to use $\omega^{\pm}(\sigma, \phi)$ [where σ is defined in Eq. (5.14)].

On the outer and intermediate scales, the shear-stress continuity condition (2.2b) becomes

$$\frac{\partial w^+}{\partial y} = \mu^{1/2}\frac{\partial w^-}{\partial Y} \quad \text{at} \quad y = 0, \qquad \frac{\partial W^+}{\partial Y} = \mu\frac{\partial W^-}{\partial Y} \quad \text{at} \quad Y = 0. \tag{7.4a,b}$$

For the total drag integral [Eqs. (2.10)], the integration interval $0 \leqslant x \leqslant 1$ now needs to be split [cf. Eqs. (5.27)] at two points δ_1 and δ_2, satisfying

$$\delta_1 \ll \mu^{1/2}, \qquad \ln\frac{1}{\delta_1} \ll \mu^{-1/2}, \qquad \mu^{1/2} \ll \delta_2 \ll 1. \tag{7.5a,b,c}$$

We therefore define $\mathcal{D} = \mathcal{D}_{\text{tip}} + \mathcal{D}_{\text{intermediate}} + \mathcal{D}_{\text{outer}}$, where the respective contributions from the tip region $(0 < x < \delta_1)$, the intermediate region $(\delta_1 < x < \delta_2)$, and the outer region $(\delta_2 < x < 1)$ are given [after changes of variables, analogous to those in Eq. (5.29)] by

$$\mathcal{D}_{\text{tip}} = \mu^{1/2}\int_{-\infty}^{-\mu^{1/2}\ln(1/\delta_1)} \left.\frac{\partial \omega^-}{\partial \phi}\right|_{\phi=0} d\sigma, \tag{7.6a}$$

$$\mathcal{D}_{\text{intermediate}} = \mu \int_{\delta_1/\mu^{1/2}}^{\delta_2/\mu^{1/2}} \left.\frac{\partial W^-}{\partial Y}\right|_{Y=0} dX, \tag{7.6b}$$

$$\mathcal{D}_{\text{outer}} = \mu^{1/2} \int_{\delta_2}^{1} \left.\frac{\partial w^-}{\partial Y}\right|_{Y=0} dx. \tag{7.6c}$$

The force balance (2.13b) is then

$$\mathcal{D}_{\text{tip}} + \mathcal{D}_{\text{intermediate}} + \mathcal{D}_{\text{outer}} = 1. \tag{7.6d}$$

Since the velocity fields are ord($\mu^{-1/2}$), we see that it is the tip and outer contributions that now contribute at leading order. The outer contribution, which is new at that order, is due to the shallowness of the groove, which has increased the shear stress from ord($\mu^{1/2}$) to ord(1). [The shear stress is also ord(1) in the intermediate region, but the horizontal extent of that region is only ord($\mu^{1/2}$).]

We now proceed with the analysis, roughly following the steps of Sec. V.

B. Leading-order slip length

As in expansions (5.6) and (5.19), we expand the velocity fields $w^\pm$, $W^\pm$, and $\omega^\pm$ in half powers of μ.

Starting again with the leading-order outer exterior solution w^+_{-1}, continuity of shear stress [Eq. (7.4a)] yields $\partial w^+_{-1}/\partial y = 0$ at $y = 0$, which is the same as before [i.e., Eq. (5.9a)]. Since the other equations governing w^+_{-1} also remain the same as in Sec. V C, the uniform solution (5.10) remains valid.

On the intermediate scale, the leading-order exterior field W^+_{-1} satisfies Laplace's equation [cf. Eq. (2.1)] and symmetry at $X = 0$ [cf. Eq. (2.5a)]. Continuity of shear stress [Eq. (7.4b)] yields $\partial W^+_{-1}/\partial Y = 0$ at $Y = 0$, while matching to the outer solution w_{-1} requires $W^+_{-1} \to \lambda_{-1}$ as $X^2 + Y^2 \to \infty$. Hence, the solution is simply an extension of Eq. (5.10),

$$W^+_{-1} \equiv \lambda_{-1}. \tag{7.7}$$

With the intermediate approximation (7.7) having the same form as the outer approximation (5.10), the leading-order inner tip approximation satisfies the same conditions as in Sec. V D, including the matching condition (5.20). Hence, the tip solutions (5.26) remains unchanged, as does their contribution (5.30) to the total drag force (7.6), i.e., $\mathcal{D}_{\text{tip}} \sim \lambda_{-1}$.

The contribution $\mathcal{D}_{\text{outer}}$ requires calculating the leading-order outer interior approximation w^-_{-1}. Laplace's equation (2.1) at leading order gives

$$\frac{\partial^2 w^-_{-1}}{\partial Y^2} = 0, \tag{7.8}$$

while no slip on the bottom [cf. Eq. (2.4b)] and continuity with the exterior approximation (5.10) [cf. Eq. (2.2a)] provide the boundary conditions

$$w^-_{-1} = 0 \quad \text{at} \quad Y = -H, \qquad w^-_{-1} = \lambda_{-1} \quad \text{at} \quad Y = 0. \tag{7.9a,b}$$

The solution is thus analogous to the shallow-groove approximation (3.1b),

$$w^-_{-1} = \lambda_{-1}\left(1 + \frac{Y}{H}\right). \tag{7.10}$$

[This solution trivially satisfies the symmetry condition at $x = 1$. It does not have to satisfy the no-slip condition (2.4a) due to the presence of the intermediate region.] Hence, the contribution (5.27b) to the drag from the outer region is

$$\mathcal{D}_{\text{outer}} \sim \frac{\lambda_{-1}}{H}. \tag{7.11}$$

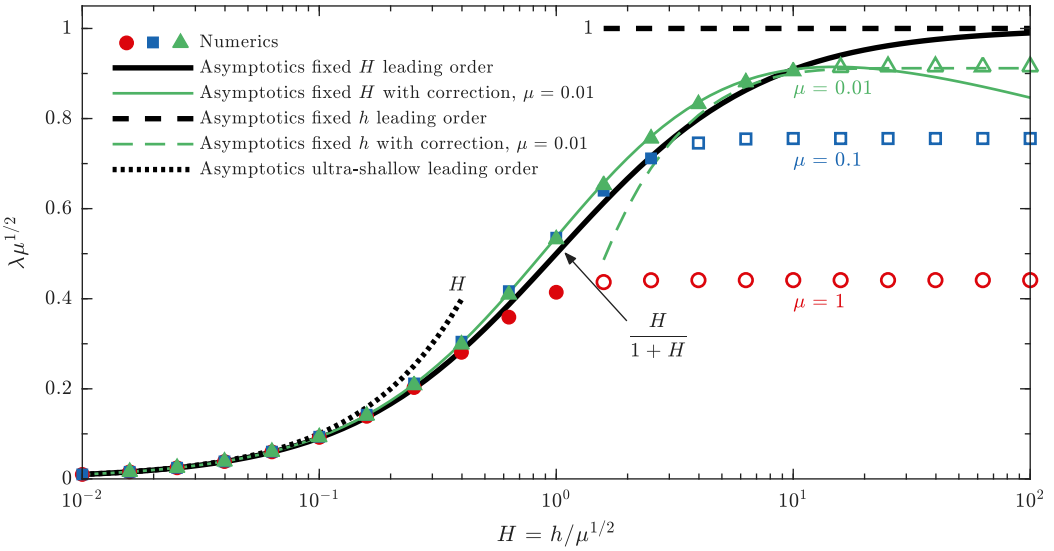


FIG. 5. Variation of the scaled slip length $\lambda\mu^{1/2}$ with scaled groove depth $H = h/\mu^{1/2}$ for various values of the viscosity ratio μ. Symbols show numerical results, with open symbols indicating $h > 1$. The thick solid curve portrays the leading-order result (7.13) in the distinguished limit $\mu, h \ll 1$ with fixed H. The thick dashed curve shows the leading-order result (5.32) in the original limit $\mu \ll 1$ with fixed h. The corresponding thin curves show the two-term approximations (7.14) and (6.30), evaluated for $\mu = 0.01$. The thick dotted curve shows the leading-order result (3.2) in the ultrashallow-groove limit $h \ll 1$ with fixed μ.

Substituting the two ord(1) contributions (5.30) and (7.11) into Eq. (7.6d) and solving for λ_{-1} yields the result

$$\lambda_{-1} = \frac{H}{1+H}, \tag{7.12}$$

from which we conclude that

$$\lambda \sim \mu^{-1/2}\frac{H}{1+H} \quad \text{for } \mu \ll 1 \text{ with fixed } H = h/\mu^{1/2}, \tag{7.13}$$

confirming the intuitively obtained leading-order result (7.1).

In Fig. 5 we show the variation of the scaled slip length $\lambda\mu^{1/2}$ with the scaled groove depth H. The thick solid curve portrays the leading-order approximation (7.12), while the symbols depict numerical solutions for various values of μ, obtained from our numerical scheme. The two agree well, provided that $h < 1$. In plotting numerical results, we employ solid symbols for $h < 1$ and open symbols for $h > 1$; in the latter case, we do not expect approximation (7.13) to hold. For perspective, we also depict (thick dashed curve) the original leading-order approximation (5.32) and (thick dotted curve) the ultrashallow-groove approximation (3.2), which are recovered by forming the respective limits $H \gg 1$ or $H \ll 1$ of Eq. (7.12). Under the rescaling of the axes, all of the aforementioned leading-order approximations are independent of μ.

C. Beyond leading-order slip length

Continuing with the distinguished limit (7.2), in Appendix D we go beyond the preceding leading-order analysis, obtaining the two-term approximation

$$\lambda \sim \mu^{-1/2}\frac{H}{1+H} + \frac{2}{\pi}\left(\frac{H}{1+H}\right)^2 \ln\frac{1}{\mu^{1/2}H} \quad \text{for } \mu \ll 1 \text{ with fixed } H = h/\mu^{1/2}. \tag{7.14}$$

We note that the second term includes contributions at both ord($\ln \mu$) and ord(1); the asymptotic error in Eq. (7.14) is *algebraically* small.

The two-term approximation (7.14) is shown as a thin solid curve in Fig. 5 for $\mu = 0.01$. As expected, it provides a better approximation than the one-term distinguished approximation (thick solid curve). For the same viscosity value, we also depict (thin dashed curve) the two-term approximation (6.30), corresponding to the original limit $\mu \ll 1$ with h fixed. It is evident that the combination of Eqs. (6.30) and (7.14) practically describes the entire range of h.

In the limit $H \ll 1$ the result (7.14) simplifies to

$$\lambda \sim \frac{h}{\mu} - \frac{h^2}{\mu^{3/2}}, \tag{7.15}$$

which constitutes an extension of the shallow-groove result (3.2). In the limit $H \gg 1$ we get

$$\lambda \sim \mu^{-1/2} - \frac{1}{h} + \frac{2}{\pi} \ln \frac{1}{h}, \tag{7.16}$$

in agreement with the small-h expansion (6.32) of the original result (6.30).

VIII. CONCLUDING REMARKS

We have investigated the canonical problem of longitudinal shear over a liquid-infused grating formed of infinitely thin ridges. With lengths normalized by the grating half period, the slip length λ depends upon two dimensionless parameters: the interior-to-exterior viscosity ratio μ and the groove depth h. This assumes that the ridges are infinitely thin, that the liquid-liquid interfaces are flat and pinned to the ridge tips, and that the flow is laminar. (Since the flow is unidirectional, the inertial terms trivially vanish for any Reynolds number [8].) Our analysis has focused on the nearly inviscid limit $\mu \ll 1$, which is singular in the above zero-solid-fraction scenario. In that limit, we have shown that λ possesses the asymptotic expansion

$$\lambda \sim \mu^{-1/2} + \lambda_0(h) \quad \text{as} \quad \mu \searrow 0, \tag{8.1}$$

where the ord(1) correction $\lambda_0(h)$ is provided by Eq. (6.29) in terms of an elliptic integral. Its small-h behavior [Eq. (6.32)] reveals a breakdown in the asymptotic expansion when h becomes comparable to $\mu^{1/2}$. Proceeding with the distinguished shallow-groove limit of $\mu \ll 1$ and $H = h/\mu^{1/2}$ fixed, we have obtained the closed-form two-term approximation (7.14), which again starts at ord($\mu^{-1/2}$) but now with the leading term depending upon H. For $H \ll 1$, namely, for extremely shallow grooves, this leading term reduces to h/μ, revealing a transition of the scaling of λ with μ across the distinguished regime. We have found excellent agreement between our asymptotic approximations and numerical solutions based upon a boundary-integral formulation.

As discussed in the Introduction, the $\mu^{-1/2}$ scaling of the effective slip length is at odds with both intuitive scaling arguments and previous heuristic models; these predict the scaling μ^{-1}, which, as noted above, is only valid for extremely shallow grooves. Our analysis reveals that the $\mu^{-1/2}$ scaling arises from a unique asymptotic structure where the velocity of both liquids varies rapidly in exponentially small regions about the tips of the infinitely thin ridges. In particular, these regions resolve the incompatibility between a uniform stream in the exterior domain—associated with an asymptotically large effective slip length and a nearly inviscid lubricant—and the need to satisfy a no-slip condition at the tips. For $\mu \ll 1$, the net viscous force supported by the liquid-liquid interface, which balances the imposed far-field shear, is dominated by the contribution from these exponentially small regions. This contradicts the naive scaling argument mentioned in the Introduction, where the viscous force was presumed to be associated with a geometric length scale, independent of μ. As the groove depth h is decreased, however, the contribution to the net viscous force from the groove scale becomes increasingly important. In fact, the distinguished limit where $H = h/\mu^{1/2}$ is held fixed corresponds to the regime where the contributions from the exponential tip regions and the groove scales become comparable. Only for extremely shallow grooves, $H \ll 1$,

does the contribution from the groove scale become dominant and the intuitive μ^{-1} scaling for the effective slip length is recovered.

Admittedly, the leading-order role played by exponentially small regions near the ridge tips suggests that the theory developed herein for infinitely thin ridges and a nearly inviscid lubricant may be sensitive to perturbations. In particular, it is clear from our analysis that even an exceedingly small solid fraction ϵ—exponentially small in μ—may induce a leading-order effect by modifying the inner problem governing those regions. More specifically, we expect finite-solid-fraction effects to become important once the ridge thickness is comparable to the exponential length scale set by the small viscosity ratio, corresponding to the condition that $\mu^{1/2}\ln\epsilon$ is of order unity. In that distinguished limit, the order of magnitude of the effective slip length must still be $\mu^{-1/2}$. At larger (but still small) solid fractions, we expect a transition to the classical $\ln\epsilon$ scaling for an inviscid lubricant [26]. Finally, for nonsmall solid fractions, the nearly inviscid limit ceases to be singular; indeed, that scenario was studied by Crowdy [25] via a regular perturbation expansion.

Another important perturbation involves our assumption that the liquid-liquid interface is pinned to the ridge tips: in some scenarios, the interface may instead lie slightly above or below them. Similar to the small-solid-fraction scenario, our analysis for infinitely thin ridges and a nearly inviscid lubricant hints to a leading-order effect once the vertical displacement of the interface becomes comparable to the exponentially small scale set by the lubricant viscosity. The case where the interface lies above the microstructure is primarily relevant to liquid-infused surfaces (SLIPS) in an "encapsulated state," which is known to facilitate high drop mobility [29]. In that case, the limit of an inviscid lubricant is singular even for a finite solid fraction, though it is intuitive that the scaling of the effective slip length would become more singular at sufficiently small solid fraction. The alternative case, where the exterior liquid partially invades the grooves, is relevant to superhydrophobic surfaces in the scenario where the liquid-gas menisci are depinned owing to a sufficiently high liquid pressure. In the latter scenario, the protrusion of the ridges into the liquid renders the inviscid-lubricant limit regular even for infinitely thin ridges [39]; the pertinent singular limit is then that of a small invasion depth [40–42].

Beyond addressing the singular perturbations discussed above, it would be valuable to extend the present theory to other microstructure geometries and flow configurations. With regards to the grating geometry, preliminary analysis suggests that the asymptotic structure of the transverse problem is similar to that found here for the longitudinal problem. However, a detailed analysis would entail solving more complex variants of the reduced Stokes-flow problems associated with this asymptotic structure (e.g., the local analysis near the tip ridges, and the driven-cavity problem)—now governed by the biharmonic equation instead of Laplace's equation. Last, we comment on another common microstructure geometry: a doubly periodic array of posts protruding from a flat solid substrate. In contrast to the grating geometry, a finite lubricant viscosity does *not* regularize here the effective-slip-length problem at zero solid fraction (i.e., infinitely thin posts). Accordingly, it would not make sense to attempt the limit process considered in this paper, of small lubricant viscosity at zero solid fraction. Instead, it would be of interest to study the asymptotic regime where both the solid fraction and the lubricant viscosity are small. This would constitute a generalization of preceding small-solid-fraction analyses of the posts configuration, which were limited to an inviscid lubricant [13,17].

DATA AVAILABILITY

The data that support the findings of this article are not publicly available upon publication because it is not technically feasible and/or the cost of preparing, depositing, and hosting the data would be prohibitive within the terms of this research project. The data are available from the authors upon reasonable request.

APPENDIX A: NUMERICAL METHOD

Our numerical method is based on expressing the velocity and shear stress at the interface in terms of an auxiliary field $q(x)$ defined on $0 < x < 1$ using boundary integrals. These relations may be expressed as linear maps M, M^+, and M^- (which are represented by matrices after discretization) satisfying

$$w^{\pm}(x,0) = M[q(x)], \qquad \frac{\partial w^-}{\partial y}(x,0) = M^-[q(x)], \qquad \frac{\partial w^+}{\partial y}(x,0) = M^+[q(x)] + 1. \tag{A1a,b,c}$$

For any given value of h, we compute these matrices. Then, we calculate $q(x)$ for any desired value of μ by solving the linear equation

$$M^+[q(x)] + 1 = \mu\, M^-[q(x)], \tag{A2}$$

representing continuity of stress (2.2b), using MATLAB's built-in matrix solver. We then evaluate $w^{\pm}(x,0)$ using Eq. (A1a), and finally obtain the slip length from relation (2.16).

1. Derivation of the boundary integrals

We first consider the interior solution, $y < 0$, for the case of infinitely deep grooves, $h = \infty$, and seek the field generated by a point source of strength -2 located on the interface at $(x, y) = (x', 0)$ where $0 < x' < 1$. In the absence of lateral boundary conditions, a solution can be written as [cf. Eq. (B4) below]

$$G_0(x - x', y) = -\frac{1}{2\pi} \ln[(x - x')^2 + y^2] + C, \tag{A3}$$

where C is an arbitrary constant. We use the method of images to construct a solution that satisfies the no-slip condition (2.4a) at $x = 0$ and symmetry condition (2.3) at $x = 1$, by adding image sources in $x < 0$ and $x > 1$ such that the resulting source distribution is antisymmetric about $x = 0$ and symmetric about $x = 1$.

Specifically, we add sources at $x = x' + 4n$ and $x = 2 - x' + 4n$ and subtract sources at $x = -x' + 4n$ and $x = -2 + x' + 4n$, where n ranges over all integers. Each of these four sets forms an array with equal spacing 4, for which the result [obtained by summing Eq. (A3) with judicious choices of C for each point, analogously to Eq. (B8)] is

$$G_4(x, y; x'') = -\frac{1}{2\pi} \ln\left[\sin^2 \frac{\pi(x - x'')}{4} + \sinh^2 \frac{\pi y}{4}\right], \tag{A4}$$

where x'' takes the values x', $2 - x'$, $-x'$, and $-2 - x'$, respectively, and a suitable value of the arbitrary additive constant has been chosen. The solution is then given by the superposition

$$G(x, y; x') = G_4(x, y; x') + G_4(x, y; 2 - x') - G_4(x, y; -x') - G_4(x, y; -2 + x'). \tag{A5}$$

[Note that changing the additive constant in Eq. (A4) does not alter this result.]

We now let $q(x')$ represent the density of point sources in $0 < x' < 1$, and construct the solution

$$w^-(x, y) = \int_0^1 G(x, y; x') q(x')\, dx', \tag{A6}$$

which satisfies Eqs. (2.1), (2.3), (2.4a), and (6.21). Thus, for $h = \infty$, the interfacial quantities can be expressed as

$$w^-(x, 0) = \int_0^1 G(x, 0; x') q(x')\, dx', \qquad \frac{\partial w^-}{\partial y}(x, 0^-) = q(x), \tag{A7a,b}$$

where

$$G(x,0;x') = \frac{1}{2\pi}\ln\frac{\sin^2\frac{\pi(x+x')}{4}\sin^2\frac{\pi(x+2-x')}{4}}{\sin^2\frac{\pi(x-x')}{4}\sin^2\frac{\pi(x+x'-2)}{4}}. \tag{A7c}$$

Considering now the case of finite h, we observe that the no-slip boundary condition (2.4b) at $y=-h$ can be satisfied by simply introducing an opposite image distribution at $y=-2h$, so we can construct the solution

$$w^-(x,y) = \int_0^1 [G(x,y;x') - G(x,-2h-y;x')]q(x')\,dx' \tag{A8}$$

to Eqs. (2.1), (2.3), and (2.4). This yields the interfacial quantities

$$w^-(x,0) = \int_0^1 [G(x,0;x') - G(x,-2h;x')]q(x')\,dx', \tag{A9a}$$

$$\frac{\partial w^-}{\partial y}(x,0) = q(x) + \int_0^1 \frac{\partial G}{\partial y}(x,-2h;x')q(x')\,dx', \tag{A9b}$$

where

$$G(x,-2h;x') = \frac{1}{2\pi}\ln\frac{g(x+x')\,g(x+2-x')}{g(x-x')\,g(x+x'-2)}, \tag{A9c}$$

$$\frac{\partial G}{\partial y}(x,-2h;x') = \frac{\coth(\pi h/2)}{4}\left[\frac{1}{g(x-x')} + \frac{1}{g(x+x'-2)} - \frac{1}{g(x+x')} - \frac{1}{g(x+2-x')}\right], \tag{A9d}$$

in which $g(x'') = 1 + [\sin^2(\pi x''/4)/\sinh^2(\pi h/2)]$. [For $h=\infty$, we have $g(x'')=1$ so that Eqs. (A9) reduce to Eqs. (A7). Hence, we no longer have to treat the case $h=\infty$ separately.]

Next, we consider the exterior solution, with $y>0$. We subtract a linear profile from w^+ to obtain a field

$$\bar{w}^+(x,y) = w^+(x,y) - y, \tag{A10}$$

which satisfies the same equations as w^+, but remains bounded as $y\to\infty$ [instead of Eq. (2.9)]. The interfacial shear stress, to be used in Eq. (2.2b), becomes

$$\frac{\partial w^+}{\partial y}(x,0) = \frac{\partial \bar{w}^+}{\partial y}(x,0) + 1. \tag{A11}$$

We treat the value of $\bar{w}^+(x,y)$ on the interface $y=0$ as given, namely, by $w^-(x,0)$ [due to continuity (2.2a)]. Since $\bar{w}^+(x,y)$ satisfies the symmetry conditions (2.5) at $x=0$ and $x=1$, the solution should involve a superposition of two arrays of point sources (of strength -2, say) with period 2, which analogously to Eq. (A4) are given by

$$G_2(x,y;x'') = -\frac{1}{2\pi}\ln\left[\sin^2\frac{\pi(x-x'')}{2} + \sinh^2\frac{\pi y}{2}\right], \tag{A12}$$

with x'' taking the values x' and $-x'$. In light of Eq. (A7b), the construction

$$\bar{w}^+(x,y) = -\frac{\partial}{\partial y}\int_0^1 [G_2(x,y;x') + G_2(x,y;-x')]w^-(x',0)\,dx' \tag{A13}$$

similarly satisfies $\bar{w}^+(x,0^+) = w^-(x,0)$, as desired. Further, it satisfies Eqs. (2.1) and (2.5), and remains bounded as $y\to\infty$, so it is the required solution.

In order to evaluate the interfacial shear of Eq. (A13), we use the fact that the integral in Eq. (A13) is harmonic, to write

$$\frac{\partial \bar{w}^+}{\partial y}(x,y) = \frac{\partial^2}{\partial x^2}\int_0^1 [G_2(x,y;x') + G_2(x,y;-x')]w^-(x',0)\,dx'. \tag{A14}$$

Although this could be evaluated directly at $y = 0$, we found that the numerical results become more accurate if we move one derivative inside the integral before taking the limit $y \searrow 0$. This yields

$$\frac{\partial \bar{w}^+}{\partial y}(x,0) = -\frac{1}{2}\frac{d}{dx}\int_0^1 \left[\cot\frac{\pi(x-x')}{2} + \cot\frac{\pi(x+x')}{2}\right] w(x',0)\,dx', \tag{A15}$$

where the Cauchy principal value is taken at the singularity $x' = x$.

Thus, the linear maps defined in Eqs. (A1) are obtained as follows: Eqs. (A9a) and (A9b) provide M and M^-, respectively, while Eq. (A15) combined with Eq. (A9b) provides M^+. It remains to detail how the system is discretized to become a matrix equation.

2. Discretization

In order to solve Eq. (A2) numerically, we need to discretize the domain $0 \leqslant x \leqslant 1$. There is no dependence on y, since the equations have been mapped onto the interface $y = 0$, with $q(x)$ being the unknown to solve for.

We use an exponentially stretched grid to resolve the small scale near the ridge tip $x = 0$. This grid is chosen to have a "relative" resolution of $\Delta = 0.002$ down to a minimum of $x_{\min} = 10^{-10}$, such that $\ln(x + x_{\min})$ ranges from $\ln(x_{\min})$ to $\ln(1 + x_{\min})$ in approximately uniform steps of Δ.

Having divided the interval $0 < x < 1$ into cells, we sample $q(x)$, $w^{\pm}(x,0)$, and $\partial w^{\pm}/\partial y(x,0)$ at the cell midpoints. The integrals in Eqs. (A9) can be directly evaluated using the midpoint rule. However, in order to improve the accuracy of Eq. (A9a), we remove the logarithmic singularity in $G(x,0;x')$ at $x' = x$ using the integral

$$\int_0^1 \frac{1}{2\pi}\ln\left[\left(\frac{4}{\pi(x-x')}\right)^2\right] q(x)\,dx' = \frac{1}{\pi}\left[1 + \ln\frac{4}{\pi} - x\ln x - (1-x)\ln(1-x)\right] q(x). \tag{A16}$$

By subtracting the integrand in Eq. (A16) from the integrand in Eq. (A9a), and then adding back the right-hand side of Eq. (A16), we obtain an expression for $w^-(x,0)$ in terms of $q(x)$ where the integrand is bounded, resulting in second-order accuracy when evaluated using the midpoint rule. In order to further increase accuracy for x close to 0 or 1 where the logarithmic singularity at $x' = -x$ or $x' = 2 - x$ is close to (albeit still outside of) the range of integration, we also perform the corresponding removal procedure for those two singularities (regardless of the value of x).

The derivative in Eq. (A15) is evaluated using central finite differences. This requires the integral to be evaluated with x at the cell boundaries. We continue to evaluate the integral using the midpoint rule, i.e., with x' at the cell midpoints. Due to x and x' being staggered in this way, direct evaluation of the integral results in the Cauchy principal value being obtained automatically for the singularity at $x' = x$. However, we improve the accuracy of the result by subtracting the identity

$$\int_0^1 \left[\cot\frac{\pi(x-x')}{2} + \cot\frac{\pi(x+x')}{2}\right] w(x,0)\,dx' = 0. \tag{A17}$$

This results in an integral of unchanged value but now finite integrand, whose numerical evaluation is again accurate to second order.

As a result of Eqs. (A16) and (A17), and the use of the midpoint method and central differencing, the resulting discrete system is accurate to second order. We have verified that this is the case, by varying Δ between 0.002 and 0.1 and checking that the error (compared with the result for the smallest value of Δ) scales like Δ^2.

For small μ, even exponential stretching is unable to resolve down to the inner scale where $\ln x = \mathrm{ord}(\mu^{-1/2})$. Hence, we make use of the local behavior [Eqs. (4.9)] and prescribe the values of $q(x)$ for $x < \sqrt{x_{\min}} = 10^{-5}$ to satisfy

$$q(x) = q(\sqrt{x_{\min}})\left(\frac{x}{\sqrt{x_{\min}}}\right)^{\alpha-1}, \qquad w(x,0) = w(\sqrt{x_{\min}},0)\left(\frac{x}{\sqrt{x_{\min}}}\right)^{\alpha}, \tag{A18a,b}$$

where $\alpha = (2/\pi)\arctan\mu^{1/2}$ is given by Eq. (4.7). Having verified that Eqs. (A18) yield accurate results for moderate values of μ when compared with the original formulation without Eqs. (A18), we then make use of Eqs. (A18) for all values of μ (even when not necessary, for simplicity).

APPENDIX B: THE CORRECTION TO THE OUTER APPROXIMATION IN THE EXTERIOR DOMAIN

We seek the harmonic function $\tilde{w}_0^+$ [defined in Eq. (6.2)] that satisfies the homogeneous Neumann conditions [cf. Eqs. (2.5) and (5.9b)]

$$\frac{\partial \tilde{w}_0^+}{\partial x} = 0 \quad \text{at} \quad x = 0, 1, \qquad \frac{\partial \tilde{w}_0^+}{\partial y} = 0 \quad \text{at} \quad y = 0, \tag{B1a,b}$$

and the far-field and tip conditions [cf. Eqs. (6.3) and (5.13)],

$$\tilde{w}_0^+ = y + o(1) \quad \text{as} \quad y \to \infty, \tag{B2a}$$

$$\tilde{w}_0^+ \sim \frac{2}{\pi}\ln\rho \quad \text{as} \quad \rho = \sqrt{x^2+y^2} \to 0. \tag{B2b}$$

We provide derivations using two different methods, as they are useful for generalizing the result for use in the other Appendixes. Both methods use the complex variable $z = x + iy$, and yield the result

$$\tilde{w}_0^+ = \frac{1}{\pi}\ln\left|4\sin^2\frac{\pi z}{2}\right| = \frac{1}{\pi}\ln\left[4\left(\sin^2\frac{\pi x}{2} + \sinh^2\frac{\pi y}{2}\right)\right], \tag{B3}$$

which clearly satisfies the required conditions (B1) and (B2).

1. Solution via method of images

We employ the fundamental solution of the 2D Laplace equation with an arbitrary additive constant C,

$$G_0(x,y) = \frac{1}{\pi}\ln(x^2+y^2) + C. \tag{B4}$$

Representing a "source of strength 4," it matches Eq. (B2b). In addition, it satisfies the Neumann conditions (B1) at $x = 0$ and at $y = 0$, but not at $x = 1$.

To obtain a solution that also satisfies the symmetry condition at $x = 1$, which together with the symmetry condition at $x = 0$ implies a period of 2, we need to superpose a periodic array of sources (B4) translated in x by $2n$, where n ranges over all integers, with the constants C chosen judiciously to avoid the series diverging. We thus posit the solution

$$\tilde{w}_0^+(x,y) = \sum_{n=-\infty}^{\infty}\left[\frac{1}{\pi}\ln[(x+2n)^2+y^2] + C_n\right], \tag{B5a}$$

with

$$C_n = -\frac{1}{\pi}\ln[(2n)^2] \quad \text{for } n \neq 0 \tag{B5b}$$

and C_0 yet to be determined. Introducing the complex variable $z = x + iy$, we rewrite Eqs. (B5) as

$$\tilde{w}_0^+(x,y) = C_0 + \frac{1}{\pi}\ln\left\{\left[\prod_{n=-\infty}^{-1}\frac{|z+2n|^2}{4n^2}\right]|z|^2\left[\prod_{n=1}^{\infty}\frac{|z+2n|^2}{4n^2}\right]\right\}. \tag{B6}$$

We pair up corresponding factors in each product to obtain

$$\tilde{w}_0^+(x,y) = C_0 + \frac{1}{\pi}\ln\left|z\prod_{n=1}^{\infty}\frac{z^2-4n^2}{4n^2}\right|^2. \tag{B7}$$

Using the Weierstrass factorization formula for the sine function, this can be rewritten as

$$\tilde{w}_0^+(x,y) = C_0 + \frac{1}{\pi}\ln\left|\frac{2}{\pi}\sin\frac{\pi z}{2}\right|^2. \tag{B8}$$

Reverting to (x, y) and choosing C_0 to satisfy the far-field condition (B2a) then yields the result (B3).

2. Solution via conformal mapping

The problem involving Eqs. (B1) and (B2), if extended symmetrically to $y < 0$, is reminiscent of the classical irrotational-flow problem of narrow-slit influx into a 2D channel, which is solved using conformal mapping in the standard textbooks [34]. We use a different mapping here, which generalizes more readily to the other problems solved in the next section.

We consider a symmetric extension about $x = 0$ to the domain $-1 < x < 1$ (with $y > 0$), resulting in the homogeneous Neumann conditions (B1) applying at the new boundaries $x = -1$, $x = 1$, and $y = 0$ (except at the singularity at the origin), while conditions (B2) are retained. We embed the harmonic $\tilde{w}_0^+$ in the complex potential

$$\Phi = \tilde{w}_0^+ + i\chi, \tag{B9}$$

which is an analytic function of $z = x + iy$, and find the appropriate solution Φ by mapping the domain $-1 < x < 1$ (with $y > 0$) to the upper half plane using the transformation [see Figs. 6(a) and 6(b)]

$$\tilde{z} = \sin\frac{\pi z}{2}, \qquad \tilde{x} = \sin\frac{\pi x}{2}\cosh\frac{\pi y}{2}, \qquad \tilde{y} = \cos\frac{\pi x}{2}\sinh\frac{\pi y}{2}. \tag{B10a,b,c}$$

The boundaries at $x = \pm 1$ and $y = 0$ map to the new real axis $\tilde{y} = 0$. In terms of the new variables (with a slight abuse of notation), $\tilde{w}_0^+$ satisfies

$$\frac{\partial \tilde{w}_0^+}{\partial \tilde{y}} = 0 \quad \text{at} \quad \tilde{y} = 0, \tag{B11a}$$

except at the origin. Conditions (B2) transform, using Eqs. (B10), to

$$\tilde{w}_0^+ = \frac{2}{\pi}\ln(2\tilde{\rho}) + o(1) \quad \text{as} \quad \tilde{\rho} \to \infty, \qquad \tilde{w}_0^+ \sim \frac{2}{\pi}\ln\tilde{\rho} \quad \text{as} \quad \tilde{\rho} \to 0, \tag{B11b,c}$$

where $\tilde{\rho} = \sqrt{\tilde{x}^2 + \tilde{y}^2} = |\tilde{z}|$. Since $\ln(2\tilde{\rho})$ is the real part of $\ln(2\tilde{z})$, which is analytic in the upper half plane, it is clear that a solution to the problem (B11) is given by

$$\Phi = \frac{2}{\pi}\ln(2\tilde{z}), \qquad \tilde{w}_0^+ = \frac{2}{\pi}\ln(2\tilde{\rho}). \tag{B12a,b}$$

Restoring z using Eq. (B10a) yields the desired result (B3).

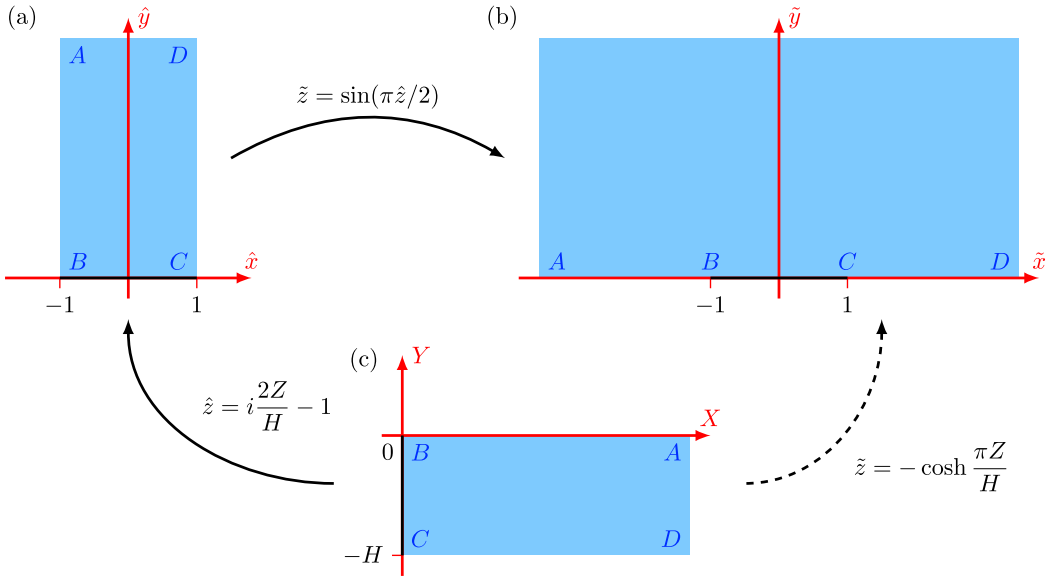


FIG. 6. Conformal maps from [(a), (c)] a semi-infinite strip to (b) the upper half plane. In Appendix B 2, (a) is mapped to (b), with $\tilde{w}_0^+$ satisfying homogeneous Neumann conditions on all boundaries (except at the origin). In Appendix C 1, (a) is mapped to (b), with Dirichlet conditions $w_{-1}^- = 0$ on AB and CD, and $w_{-1}^- = 1$ on BC. In Appendix D 3, (c) is mapped via (a) to (b), with Dirichlet conditions $W_{-1}^- = 1$ on AB and $W_{-1}^- = 0$ on BC and CD.

APPENDIX C: LEADING-ORDER OUTER APPROXIMATION IN THE INTERIOR DOMAIN

In order to calculate the leading-order outer interior flow w_{-1}^- for Sec. VI D, we introduce a shifted horizontal coordinate and flipped vertical coordinate,

$$\hat{x} = x - 1, \qquad \hat{y} = -y, \tag{C1a,b}$$

and consider a full groove $-1 < \hat{x} < 1$ (with $\hat{y} > 0$) instead of imposing the symmetry condition (2.5b) at $\hat{x} = 0$. Thus, with a slight abuse of notation, we seek a harmonic function $w_{-1}^-(\hat{x}, \hat{y})$ satisfying the Dirichlet conditions [cf. Eqs. (2.4) and (6.20)]

$$w_{-1}^- = 0 \quad \text{at} \quad \hat{x} = \pm 1 \quad \text{and at} \quad \hat{y} = h, \qquad w_{-1}^- = 1 \quad \text{at} \quad \hat{y} = 0. \tag{C2a,b}$$

We use conformal mapping as in Appendix B 2, and embed w_{-1}^- in a complex potential

$$\Phi = w_{-1}^- + i\chi, \tag{C3}$$

a function of $\hat{z} = \hat{x} + i\hat{y}$.

1. Infinitely deep grooves

In the limit of infinitely deep grooves, $h = \infty$, the no-slip condition at $\hat{y} = h$ is replaced by a decay condition as $\hat{y} \to \infty$ [see Eq. (6.21)]. The resulting problem appears in standard textbooks, e.g., as a heat conduction problem in a semi-infinite slab whose end is held at an elevated temperature compared with its sides [34]. The solution is described here briefly for completeness.

We again map the semi-infinite strip to the upper half plane via the transformation $\tilde{z} = \sin(\pi\hat{z}/2)$ [analogous to Eqs. (B10), illustrated in Fig. 6]. Since Dirichlet conditions are conformally invariant, Eqs. (C2) become

$$w_{-1}^-(\tilde{x}, 0) = \begin{cases} 0 & \text{for} \quad |\tilde{x}| > 1 \\ 1 & \text{for} \quad |\tilde{x}| < 1, \end{cases} \qquad w_{-1}^- \to 0 \quad \text{as} \quad \tilde{\rho} \to \infty. \tag{C4a,b}$$

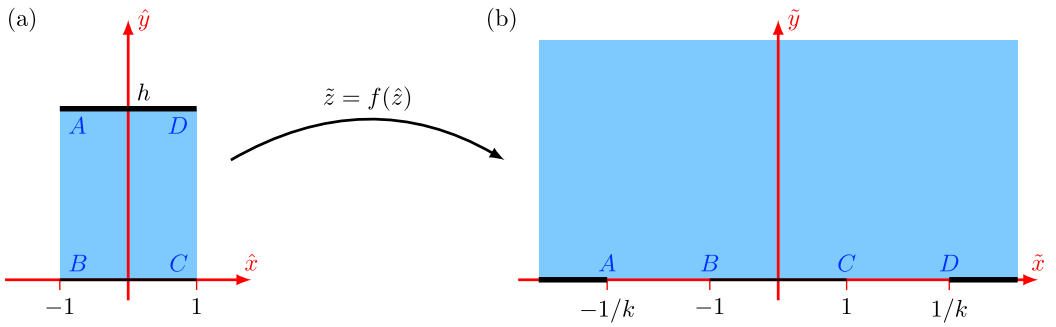


FIG. 7. Conformal map from a rectangle to the upper half plane used in Appendix C 2, whose inverse is a Schwarz-Christoffel map [Eq. (C8)]. The boundary conditions are $w_{-1}^- = 0$ on all boundaries except BC, where $w_{-1}^- = 1$ instead.

Since the imaginary part of $\log\tilde{z} = \ln\tilde{\rho} + i\arg\tilde{z}$ takes the values 0 and π on the two halves of the real axis, it is clear that a solution to Eqs. (C4) can be constructed as

$$\Phi = \frac{1}{i\pi}[\log(\tilde{z}-1) - \log(\tilde{z}+1)], \tag{C5a}$$

$$w_{-1}^- = \frac{1}{\pi}\arg\frac{\tilde{z}-1}{\tilde{z}+1}, \tag{C5b}$$

Converting to real form and reverting to $\hat{x}$ and $\hat{y}$ using the analog of Eqs. (B10) then yields

$$w_{-1}^- = \frac{1}{\pi}\arctan\frac{2\tilde{y}}{\tilde{x}^2+\tilde{y}^2-1} \tag{C6a}$$

$$= \frac{1}{\pi}\arctan\frac{2\cos\frac{\pi\hat{x}}{2}\sinh\frac{\pi\hat{y}}{2}}{\sin^2\frac{\pi\hat{x}}{2}+\sinh^2\frac{\pi\hat{y}}{2}-1}, \tag{C6b}$$

where the range of the arctangent is taken to be 0 to π. We can then evaluate the interfacial shear for $-1 < \hat{x} < 1$ as

$$-\left.\frac{\partial w_{-1}^-}{\partial\hat{y}}\right|_{\hat{y}=0} = \frac{1}{\cos(\pi\hat{x}/2)}, \tag{C7}$$

from which Eq. (6.22) follows.

2. Arbitrary groove depth

For an arbitrary groove depth h, we need the map $\tilde{z} = f(\hat{z})$ from the rectangular domain $-1 < \hat{x} < 1$, $0 < \hat{y} < h$ to the upper half plane $\tilde{y} > 0$ (see Fig. 7). This is the inverse of a Schwarz-Christoffel map (e.g. Ref. [34]), which due to symmetry in $\hat{x}$ and $\tilde{x}$ has the form

$$\hat{z} = f^{-1}(\tilde{z}) = -M\int_0^{\tilde{z}} \frac{dv}{(v+1/k)^{1/2}(v+1)^{1/2}(v-1)^{1/2}(v-1/k)^{1/2}}, \tag{C8}$$

where the positive real constants M and k remain to be determined. We express f^{-1} in terms of the incomplete and complete elliptic integrals of the first kind with parameter $m = k^2$, defined by

$$\mathrm{F}(\tilde{z};m) = \int_0^{\tilde{z}} \frac{dv}{(1-v^2)^{1/2}(1-mv^2)^{1/2}}, \qquad \mathrm{K}(m) = \mathrm{F}(1;m). \tag{C9a,b}$$

Comparison of Eqs. (C8) and (C9a) reveals that $f^{-1}(\tilde{z}) = kM\mathrm{F}(\tilde{z};k^2)$. Next, the mapping of point D in Fig. 7 yields the condition $1 + ih = f(1/k)$, which after splitting the integral at $v = 1$ and

separating the real and imaginary parts becomes

$$1 = kM\mathrm{K}(k^2), \quad h = kM\mathrm{K}(1-k^2). \tag{C10}$$

Eliminating M, we deduce that k depends on h according to the equation

$$\frac{\mathrm{K}(1-k^2)}{\mathrm{K}(k^2)} = h, \tag{C11}$$

and the (inverse) mapping (C8) can be expressed as

$$\hat{z} = f^{-1}(\tilde{z}) = \frac{\mathrm{F}(\tilde{z};k^2)}{\mathrm{K}(k^2)}. \tag{C12}$$

The inverse of the function $\mathrm{F}(\,\cdot\,;k^2)$ is the Jacobi elliptic sine function with parameter $m = k^2$, denoted $\mathrm{sn}(\,\cdot\,,k^2)$. Using this, we can express the forward mapping as

$$\tilde{z} = f(\hat{z}) = \mathrm{sn}(\mathrm{K}(k^2)\hat{z};k^2). \tag{C13}$$

Next, we need to solve for w_{-1}^- in the upper half $\tilde{z}$ plane. The interface on which $w_{-1}^- = 1$ is mapped is from $\hat{y} = 0$ with $-1 < \hat{x} < 1$ to $\tilde{y} = 0$ with $-1 < \tilde{x} < 1$ (see Fig. 7). The remaining portions of the rectangular boundary, on which $w_{-1}^- = 0$, are mapped to the remainder of the real axis. Hence, in the $\tilde{z}$ plane, w_{-1}^- again satisfies the Dirichlet conditions (C4), and the solution for w_{-1}^- is thus given by Eqs. (C5).

The interfacial shear, however, is not given by Eq. (C7), since the mapping (C13) is different. From the chain rule, $\partial w_{-1}^-/\partial\hat{z} = (df/d\hat{z})(\partial w_{-1}^-/\partial\tilde{z})$, the shear is

$$-\left.\frac{\partial w_{-1}^-}{\partial\hat{y}}\right|_{\hat{y}=0} = \frac{2}{\pi}\frac{1}{1-f^2(\hat{x})}\frac{df(\hat{x})}{d\hat{x}}. \tag{C14}$$

Hence, the sought regularized drag integral (6.17) becomes

$$\mathcal{F} = \frac{2}{\pi}\int_{-1}^{0}\left[\frac{1}{1-f^2(\hat{x})}\frac{df(\hat{x})}{d\hat{x}} - \frac{1}{\hat{x}+1}\right]d\hat{x} \tag{C15a}$$

$$= \frac{2}{\pi}\lim_{\hat{x}\to-1}\left[\frac{1}{2}\ln\frac{1-f(\hat{x})}{1+f(\hat{x})} + \ln(\hat{x}+1)\right]. \tag{C15b}$$

To calculate the limit, we use Eqs. (C12) and (C9) to obtain

$$f^{-1}(-1+\varepsilon) \sim -1 + \frac{\sqrt{2\varepsilon}}{\mathrm{K}(k^2)\sqrt{1-k^2}} \quad \text{as} \quad \varepsilon \searrow 0, \tag{C16}$$

whereby

$$f(\hat{x}) \sim -1 + \frac{1-k^2}{2}\mathrm{K}^2(k^2)(1+\hat{x})^2 \quad \text{as} \quad \hat{x} \searrow -1. \tag{C17}$$

Substitution into Eq. (C15b) then yields the result (6.27).

APPENDIX D: HIGHER-ORDER APPROXIMATION FOR THE SLIP LENGTH IN THE DISTINGUISHED SHALLOW-GROOVE LIMIT

We seek to calculate the asymptotic correction to the leading-order result (7.12) in the distinguished limit for shallow grooves (Sec. VII). We proceed to calculate the solution fields required to determine $\mathcal{D}_{\mathrm{tip}}$, $\mathcal{D}_{\mathrm{outer}}$, and $\mathcal{D}_{\mathrm{intermediate}}$ to $\mathrm{ord}(\mu^{1/2})$. Following Fraenkel [43], we group together terms that are separated only by a logarithmic factor (in μ), and ensure that all approximations involve discarding terms that are algebraically small.

1. Higher-order outer approximation in the exterior domain and inner approximation near the tip

We start by considering the ord(1) outer-scale problem in the exterior domain. Like in the calculation for fixed h (see Sec. VI), the field $w_0^+(x, y)$ satisfies Laplace's equation [cf. Eq. (2.1)], homogeneous Neumann conditions at $x = 0$ and $x = 1$ [cf. Eqs. (2.5)], and the far-field condition (6.3). However, matching shear stress (7.4a) with the leading-order interior solution (7.10) now provides an inhomogeneous Neumann condition

$$\frac{\partial w_0^+}{\partial y} = \frac{\lambda_{-1}}{H} \quad \text{at} \quad y = 0. \tag{D1}$$

Since this shear stress contributes to the drag, the contribution from the corner singularity reduces from 1 to λ_{-1}, so instead of Eq. (5.13) we have

$$w_0^+ \sim \frac{2}{\pi}\lambda_{-1} \ln \rho \quad \text{as} \quad \rho \to 0. \tag{D2}$$

Indeed, this condition can also be derived by matching via the intermediate region to the tip solution (5.26a), whose amplitude is λ_{-1}.

Upon subtracting the shear $(\lambda_{-1}/H)y$ and the far-field constant λ_0 from w_0^+, we recover a rescaled form of the problem for $\tilde{w}_0^+$ that was solved in Appendix B. Hence, the required solution is

$$w_0^+ = \lambda_{-1}\tilde{w}_0^+ + \frac{\lambda_{-1}}{H}y + \lambda_0, \tag{D3}$$

where $\tilde{w}_0^+$ is given by Eq. (B3). In particular, the local behavior near the tip is

$$w_0^+ \sim \lambda_{-1}\left(\frac{2}{\pi}\ln \rho + \beta\right) + \lambda_0, \tag{D4}$$

where β is (the pure number) given by Eq. (6.7).

Next, on the intermediate scale at ord(1), the field $W_0^+(X, Y)$ satisfies Laplace's equation [cf. Eq. (2.1)], homogeneous Neumann conditions at $X = 0$ and $Y = 0$ [cf. Eqs. (2.5a) and (7.4b)], and asymptotic matching to the outer solution (D4) in the form

$$W_0^+ \sim \lambda_{-1}\left[\frac{2}{\pi}\ln(\mu^{1/2}R) + \beta\right] + \lambda_0 \quad \text{as} \quad R \to \infty, \tag{D5}$$

where $R = \sqrt{X^2 + Y^2}$. We conclude that the solution is simply an extrapolation of the outer solution (D3) [cf. Eq. (7.7)],

$$W_0^+ = \lambda_{-1}\left[\frac{2}{\pi}\ln(\mu^{1/2}R) + \beta\right] + \lambda_0. \tag{D6}$$

Finally, on the tip scale at ord(1), the general solution (6.8) remains valid. Employing a 2-2 van Dyke matching between ω^+ and W^+ [cf. Eq. (6.9)], we determine the constant

$$C_0 = \lambda_{-1}\beta + \lambda_0. \tag{D7}$$

Hence, the result (6.10) for $\omega_0^\pm$ remains valid, except with a factor λ_{-1} multiplying β.

2. Correction to the outer solution in the interior domain

We now consider the ord(1) outer-scale problem in the interior domain. As in the leading-order calculation [see Eqs. (7.8) and (7.9)], the field w_0^- satisfies $\partial^2 w_0^-/\partial Y^2 = 0$ with the no-slip condition $w_0^- = 0$ at $Y = -H$. Here, the interfacial condition follows from continuity with Eqs. (D3),

$$w_0^- = \lambda_{-1}\tilde{w}_0^+(x, 0) + \lambda_0 \quad \text{at} \quad Y = 0. \tag{D8}$$

The solution (7.10) is then simply modified to

$$w_0^- = [\lambda_{-1}\tilde{w}_0^+(x,0) + \lambda_0]\left(1 + \frac{Y}{H}\right). \tag{D9}$$

Similarly to the leading-order calculation, the symmetry condition at $x = 1$ is identically satisfied (given the symmetry of $\tilde{w}_0^+$), while the symmetry condition at $x = 0$ does not need to be satisfied due to the presence of an intervening intermediate region.

3. Leading-order intermediate-scale approximation in the interior domain

We follow with the leading-order interior problem in the intermediate region. The field W_{-1}^- satisfies Laplace's equation in the (X, Y) coordinates [cf. Eq. (2.1)] and the no-slip conditions [cf. Eqs. (2.4)]

$$W_{-1}^- = 0 \quad \text{at} \quad X = 0, \qquad W_{-1}^- = 0 \quad \text{at} \quad Y = -H. \tag{D10a,b}$$

Further, making use of the uniform exterior approximation (7.7) and the velocity-continuity condition (2.2a) yields

$$W_{-1}^- = \lambda_{-1} \quad \text{at} \quad Y = 0, \tag{D10c}$$

while matching to the outer approximation (7.10) requires

$$W_{-1}^- \sim \lambda_{-1}\left(1 + \frac{Y}{H}\right) \quad \text{as} \quad X \to \infty. \tag{D11}$$

As in Eqs. (B9) and (C3), we embed W_{-1}^- in a complex potential,

$$\Phi = W_{-1}^- + i\chi, \tag{D12}$$

which must be an analytic function of $Z = X + iY$, in the horizontal semi-infinite strip $X > 0$, $-H < Y < 0$. We use the conformal map $\hat{z} = i(2Z/H) - 1$ to rotate and stretch this strip to the previously used semi-infinite strip (Fig. 6), which is then again mapped to the upper half plane using $\tilde{z} = \sin(\pi\hat{Z}/2)$. Thus, the overall map is given by

$$\tilde{z} = -\cosh\frac{\pi Z}{H}, \qquad \tilde{x} = -\cosh\frac{\pi X}{H}\cos\frac{\pi Y}{H}, \qquad \tilde{y} = -\sinh\frac{\pi X}{H}\sin\frac{\pi Y}{H}. \tag{D13a,b,c}$$

The Dirichlet conditions (D10) and the matching conditions (D11) become

$$W_{-1}^-(\tilde{x},0) = \begin{cases} \lambda_{-1} & \text{for} \quad \tilde{x} < -1 \\ 0 & \text{for} \quad \tilde{x} > -1, \end{cases} \qquad W_{-1}^- \sim \lambda_{-1}\frac{\arg\tilde{z}}{\pi} \quad \text{as} \quad |\tilde{z}| \to \infty. \tag{D14a,b}$$

The solution is thus given by

$$\Phi = \frac{\lambda_{-1}}{i\pi}\log(1+\tilde{z}), \qquad W_{-1}^- = \frac{\lambda_{-1}}{\pi}\arg(1+\tilde{z}). \tag{D15a,b}$$

Reverting to (X, Y) using Eqs. (D13) gives

$$W_{-1}^- = \frac{\lambda_{-1}}{\pi}\arctan\frac{\sinh(\pi X/H)\sin(\pi Y/H)}{\cosh(\pi X/H)\cos(\pi Y/H) - 1}, \tag{D16}$$

where the range of the arctangent is taken to be 0 to π. The interfacial shear is then

$$\left.\frac{\partial W_{-1}^-}{\partial Y}\right|_{Y=0} = \frac{\lambda_{-1}}{H}\coth\frac{\pi X}{2H}. \tag{D17}$$

4. Drag and slip length

We now calculate the contributions to the drag, Eqs. (7.6), up to and including ord($\mu^{1/2}$). Using Eq. (D7), the tip contribution (7.6a) is analogous to Eq. (6.13) but with factors of λ_{-1} inserted:

$$\mathcal{D}_{\text{tip}} \sim \lambda_{-1} + \mu^{1/2}\left(-\frac{2}{\pi}\lambda_1 \ln\frac{1}{\delta_1} + \lambda_{-1}\beta + \lambda_0\right). \tag{D18}$$

The intermediate contribution (7.6b) is, using Eq. (D17),

$$\mathcal{D}_{\text{intermediate}} \sim \mu^{1/2}\int_{\delta_1/\mu^{1/2}}^{\delta_2/\mu^{1/2}} \frac{\lambda_{-1}}{H}\coth\frac{\pi X}{2H}\,dX \tag{D19a}$$

$$= \mu^{1/2}\frac{2\lambda_{-1}}{\pi}\ln\frac{\sinh[\pi\delta_2/(2H\mu^{1/2})]}{\sinh[\pi\delta_1/(2H\mu^{1/2})]}. \tag{D19b}$$

Since $\delta_1 \ll \mu^{1/2} \ll \delta_2$ [see Eqs. (7.5)], we can expand this as

$$\mathcal{D}_{\text{intermediate}} \sim \lambda_{-1}\left(\frac{\delta_2}{H} + \mu^{1/2}\frac{2}{\pi}\ln\frac{H\mu^{1/2}}{\pi\delta_1}\right). \tag{D20}$$

Finally, for the outer contribution (7.6c), the solutions (7.10) and (D9) yield

$$\mathcal{D}_{\text{outer}} \sim \int_{\delta_2}^{1}\left[\frac{\lambda_{-1}}{H} + \mu^{1/2}\frac{\lambda_{-1}\tilde{w}_0^+(x,0)+\lambda_0}{H}\right]dx. \tag{D21}$$

Using Eq. (B3), we find that $\int_0^1 \tilde{w}_0^+(x,0)\,dx = 0$, so we are left with

$$\mathcal{D}_{\text{outer}} \sim \frac{\lambda_{-1}}{H}(1-\delta_2) + \mu^{1/2}\frac{\lambda_0}{H}. \tag{D22}$$

Adding together Eqs. (D18), (D20), and (D22), the terms involving δ_1 and δ_2 cancel as expected, and we obtain the total drag,

$$\mathcal{D} \sim \lambda_{-1}\left(1+\frac{1}{H}\right) + \mu^{1/2}\left[\lambda_{-1}\frac{2}{\pi}\ln(H\mu^{1/2}) + \lambda_0\left(1+\frac{1}{H}\right)\right], \tag{D23}$$

where the error is algebraically small. Requiring that the ord($\mu^{1/2}$) term vanishes [cf. Eq. (7.6d)], we conclude that

$$\lambda_0 = \frac{2\lambda_{-1}}{\pi}\left(\frac{H}{1+H}\right)\ln\frac{1}{\mu^{1/2}H}. \tag{D24}$$

Substitution of Eq. (7.12) into Eq. (D24) furnishes the requisite formula (7.14).

[1] J. P. Rothstein, Slip on superhydrophobic surfaces, Annu. Rev. Fluid Mech. **42**, 89 (2010).
[2] L. Bocquet and E. Lauga, A smooth future? Nat. Mater. **10**, 334 (2011).
[3] D. Quéré, Wetting and roughness, Annu. Rev. Mater. Res. **38**, 71 (2008).
[4] A. Lafuma and D. Quéré, Slippery pre-suffused surfaces, Europhys. Lett. **96**, 56001 (2011).
[5] T.-S. Wong, S. H. Kang, S. K. Y. Tang, E. J. Smythe, B. D. Hatton, A. Grinthal, and J. Aizenberg, Bioinspired self-repairing slippery surfaces with pressure-stable omniphobicity, Nature (London) **477**, 443 (2011).
[6] S. Hardt and G. McHale, Flow and drop transport along liquid-infused surfaces, Annu. Rev. Fluid Mech. **54**, 83 (2022).
[7] A. M. J. Davis and E. Lauga, Geometric transition in friction for flow over a bubble mattress, Phys. Fluids **21**, 011701 (2009).

[8] G. K. Batchelor, *An Introduction to Fluid Dynamics* (Cambridge University Press, Cambridge, UK, 1967).
[9] J. R. Philip, Integral properties of flows satisfying mixed no-slip and no-shear conditions, Z. Angew. Math. Phys. **23**, 960 (1972).
[10] E. Lauga and H. A. Stone, Effective slip in pressure-driven Stokes flow, J. Fluid Mech. **489**, 55 (2003).
[11] C. Ybert, C. Barentin, C. Cottin-Bizonne, P. Joseph, and L. Bocquet, Achieving large slip with superhydrophobic surfaces: Scaling laws for generic geometries, Phys. Fluids **19**, 123601 (2007).
[12] A. M. J. Davis and E. Lauga, The friction of a mesh-like super-hydrophobic surface, Phys. Fluids **21**, 113101 (2009).
[13] A. M. J. Davis and E. Lauga, Hydrodynamic friction of fakir-like superhydrophobic surfaces, J. Fluid Mech. **661**, 402 (2010).
[14] O. Schnitzer, Singular effective slip length for longitudinal flow over a dense bubble mattress, Phys. Rev. Fluids **1**, 052101(R) (2016).
[15] O. Schnitzer, Slip length for longitudinal shear flow over an arbitrary-protrusion-angle bubble mattress: The small-solid-fraction singularity, J. Fluid Mech. **820**, 580 (2017).
[16] E. Yariv, Velocity amplification in pressure-driven flows between superhydrophobic gratings of small solid fraction, Soft Matter **13**, 6287 (2017).
[17] O. Schnitzer and E. Yariv, Small-solid-fraction approximations for the slip-length tensor of micropillared superhydrophobic surfaces, J. Fluid Mech. **843**, 637 (2018).
[18] O. Schnitzer and E. Yariv, Resistive-force theory for mesh-like superhydrophobic surfaces, Phys. Rev. Fluids **3**, 032201(R) (2018).
[19] E. Yariv and O. Schnitzer, Pressure-driven plug flows between superhydrophobic surfaces of closely spaced circular bubbles, J. Eng. Math. **111**, 15 (2018).
[20] C.-H. Choi and C.-J. Kim, Large slip of aqueous liquid flow over a nanoengineered superhydrophobic surface, Phys. Rev. Lett. **96**, 066001 (2006).
[21] C. Lee, C.-H. Choi, and C.-J. Kim, Structured surfaces for a giant liquid slip, Phys. Rev. Lett. **101**, 064501 (2008).
[22] C. W. Extrand, Criteria for ultralyophobic surfaces, Langmuir **20**, 5013 (2004).
[23] M. Sbragaglia, A. M. Peters, C. Pirat, B. M. Borkent, R. G. H. Lammertink, M. Wessling, and D. Lohse, Spontaneous breakdown of superhydrophobicity, Phys. Rev. Lett. **99**, 156001 (2007).
[24] C. Lee, C.-H. Choi, and C.-J. Kim, Superhydrophobic drag reduction in laminar flows: A critical review, Exp. Fluids **57**, 176 (2016).
[25] D. G. Crowdy, Perturbation analysis of subphase gas and meniscus curvature effects for longitudinal flows over superhydrophobic surfaces, J. Fluid Mech. **822**, 307 (2017).
[26] J. R. Philip, Flows satisfying mixed no-slip and no-shear conditions, Z. Angew. Math. Phys. **23**, 353 (1972).
[27] C. Schönecker, T. Baier, and S. Hardt, Influence of the enclosed fluid on the flow over a microstructured surface in the Cassie state, J. Fluid Mech. **740**, 168 (2014).
[28] T. V. Nizkaya, E. S. Asmolov, and O. I. Vinogradova, Gas cushion model and hydrodynamic boundary conditions for superhydrophobic textures, Phys. Rev. E **90**, 043017 (2014).
[29] J. D. Smith, R. Dhiman, S. Anand, E. Reza-Garduno, R. E. Cohen, G. H. McKinley, and K. K. Varanasi, Droplet mobility on lubricant-impregnated surfaces, Soft Matter **9**, 1772 (2013).
[30] L. M. Hocking, A moving fluid interface on a rough surface, J. Fluid Mech. **76**, 801 (1976).
[31] D. W. Bechert and M. Bartenwerfer, The viscous flow on surfaces with longitudinal ribs, J. Fluid Mech. **206**, 105 (1989).
[32] Z. Yan and K. N. Kowal, A controllable sliding law for thin-film flows over slippery fluid-saturated substrates: Theory and experiments, J. Fluid Mech. **982**, A14 (2024).
[33] E. J. Hinch, *Perturbation Methods* (Cambridge University Press, Cambridge, UK, 1991).
[34] J. W. Brown and R. V. Churchill, *Complex Variables and Applications* (McGraw-Hill, New York, 2003).
[35] M. Van Dyke, *Perturbation Methods in Fluid Mechanics* (Academic Press, New York, 1964).
[36] D. E. Cormack, L. G. Leal, and J. J. Imberger, Natural convection in a shallow cavity with differentially heated end walls. Part 1. Asymptotic theory, J. Fluid Mech. **65**, 209 (1974).

[37] A. K. Sen and S. H. Davis, Steady thermocapillary flows in two-dimensional slots, J. Fluid Mech. **121**, 163 (1982).
[38] M. Abramowitz and I. A. Stegun, *Handbook of Mathematical Functions*, 3rd ed. (Dover, New York, 1965).
[39] D. G. Crowdy, Slip length formulas for longitudinal shear flow over a superhydrophobic grating with partially filled cavities, J. Fluid Mech. **925**, R2 (2021).
[40] E. Yariv, Effective slip length for transverse shear flow over partially-invaded grooves, J. Fluid Mech. **957**, R1 (2023).
[41] E. Yariv, Highly singular slip length for longitudinal shear flow over a dense bubble mattress, J. Fluid Mech. **967**, R3 (2023).
[42] E. Yariv, Longitudinal shear flow over a superhydrophobic grating with partially invaded grooves and curved menisci, SIAM J. Appl. Math. **84**, 1186 (2024).
[43] L. E. Fraenkel, On the methods of matched asymptotic expansions. Part I: A matching principle, Math. Proc. Cambridge Philos. Soc. **65**, 209 (1969).